



Lindel, F., Bennett, R. and Buhmann, S.Y. (2021) Macroscopic quantum electrodynamics approach to nonlinear optics and application to polaritonic quantum-vacuum detection. *Physical Review A: Atomic, Molecular and Optical Physics*, 103(3), 033705. (doi: [10.1103/PhysRevA.103.033705](https://doi.org/10.1103/PhysRevA.103.033705)).

This is the author's final accepted version.

There may be differences between this version and the published version. You are advised to consult the publisher's version if you wish to cite from it.

<http://eprints.gla.ac.uk/258861/>

Deposited on: 17 November 2021

Enlighten – Research publications by members of the University of Glasgow
<http://eprints.gla.ac.uk>

Macroscopic quantum electrodynamics approach to nonlinear optics and application to polaritonic quantum-vacuum detection

Frieder Lindel¹, Robert Bennett², and Stefan Yoshi Buhmann³

¹ *Physikalisches Institut, Albert-Ludwigs-Universität Freiburg, Hermann-Herder-Straße 3, 79104 Freiburg, Germany*

² *School of Physics and Astronomy, University of Glasgow, Glasgow G12 8QQ, United Kingdom*

³ *Institut für Physik, Universität Kassel, Heinrich-Plett Straße 40, 34132 Kassel, Germany*

(Dated: February 15, 2021)

We provide an in-depth discussion of a theoretical framework recently introduced [Lindel *et al.* Phys. Rev. A **102**, 041701(R) (2020)] which is capable of predicting the electromagnetic field emerging from a nonlinear crystal through which a coherent laser pulse is shone. This framework is based on macroscopic quantum electrodynamics and includes dispersion and absorption effects inside the crystal and allows for arbitrary optical environments through the classical Green's tensor. We introduce a diagrammatic approach with which the nonlinear processes contributing to the electric field operator up to certain orders in the perturbation series can be represented in a convenient way. Applying this framework to the setup of electro-optic sampling experiments of the polaritonic quantum vacuum, we derive analytical results for the electro-optic sampling between distinct spatio-temporal regions. Also, we discuss different approximations and the parameter ranges in which they apply including angled or diverging beams, thermal fluctuations, as well as (linear) absorption effects upon the polaritonic quantum vacuum. Finally, we compare these theoretical results to experimental data.

I. INTRODUCTION

According to quantum mechanics, two canonically conjugate variables cannot be measured simultaneously with arbitrary precision [1]. This seemingly technical statement has far-reaching consequences, one of the most fascinating being that the ground state of quantum electrodynamics (QED) is endowed with a rich structure: electromagnetic fluctuations persist even in empty space. Since these so called vacuum fluctuations interact with matter just as any other electromagnetic field does, indirect evidence for their existence is found in a variety of contexts. For example, the spontaneous emission of an atom can be described as an interaction with fluctuating vacuum fields [2, 3], just as the Casimir force [4], Lamb shift [5], and resonant energy transfer [6] can be seen as originating from the existence of ground-state fluctuations.

As always in electrodynamics, the relation between fields and charges is reciprocal—above we described the quantum fluctuations of the electromagnetic field affecting atoms or macroscopic objects, but one can also take the opposite point of view, finding that the structure of the fluctuating quantum ground state is modified by the presence of matter. In other words, the interaction of light and matter also leads to a new ground state of the composite light-matter system. This more structured ground state consisting of the coupled system of light and matter is usually referred to as the *polaritonic* or *medium-assisted* ground state. The matter-induced changes in the quantum ground state can again be accessed indirectly by e.g. measuring the spontaneous decay rate of an atom in close proximity to a macroscopic body [7] or by measuring Casimir-Polder forces [8].

Recently, a new route to detecting the quantum vacuum has been realized [9, 10] by means of electro-optic sampling [11, 12]. The idea is based on the

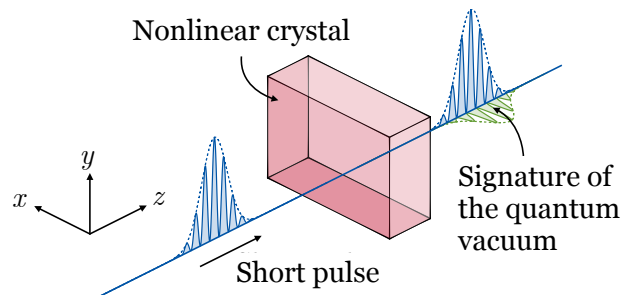


Figure 1. *Schematic illustration of the working principle of electro-optic sampling experiments: A linearly polarised short laser pulse (blue) propagates through a nonlinear crystal. Inside the crystal, the pulse mixes with the quantum fluctuations of the electro-magnetic field leading to a new, differently polarised contribution to the field (green). Since, this new contribution carries information about the quantum vacuum the latter can be accessed by analysing the field emerging from the crystal.*

fact that two electric fields inside nonlinear media can effectively interact—a conclusion which also holds for the quantum vacuum fluctuations since these interact with matter in the same way as any other type of field. Hence, an ultra short laser pulse propagating through a nonlinear crystal interacts with the quantum vacuum via the nonlinear medium, which leads to a change in the polarization of the probe pulse emerging from the crystal. Analyzing this polarisation change, one can obtain information about the polaritonic ground state. Upon using two laser pulses instead of one, one is further able to access field correlations of the electromagnetic quantum vacuum between distinct spatio-temporal regions as recently demonstrated in Ref. [10].

Interactions and mixing of electromagnetic fields which involve the quantum vacuum are also familiar from other phenomena of nonlinear quantum optics,

for example spontaneous parametric down-conversion [13] or photonic Bose–Einstein condensates [14]. Given the different nonlinear processes which include the quantum vacuum as a key actor, a theory of nonlinear optics which includes the full medium-assisted quantum vacuum is needed. In particular, given that both ultrashort laser pulses and vacuum fluctuations are broadband phenomena in frequency space, this theory has to account for dispersion and, as required by the Kramers–Kronig relations, absorption of all materials involved. We have recently developed such a theory in order to find the output statistics of electro-optic sampling experiments, showing how these experiments can be used to reveal different characteristics of the medium-assisted quantum vacuum [18] such as longitudinal and transverse fluctuating fields. In this theory, the description of the polaritonic quantum vacuum is provided by macroscopic QED in dispersing and absorbing media [15, 16], which can be equivalently obtained by canonically quantising classical electrodynamics in media by Fano diagonalisation of appropriate collections of coupled oscillators [17], or by taking a phenomenological approach [15, 16], constrained by consistency with the fluctuation-dissipation theorem, the commutation relations of QED, and classical electrodynamics in the appropriate limit.

Here, in Sec. II we firstly extend the discussion of the theoretical framework provided in Ref. [18] which is capable of predicting the electric field operator behind a nonlinear crystal through which a coherent laser pulse is propagated accounting for absorption, dispersion, general nonlinear media an arbitrary optical environments via the Green’s tensor. This especially includes a new diagrammatic representation which can be used as a convenient tool to apply this theoretical framework to different setups and geometries in which the nonlinear interaction of the polaritonic ground state with a coherent laser field is considered. We demonstrate the utility of this diagrammatic approach by using it to re-derive the detector statistics of electro-optic sampling experiments of the quantum vacuum in Sec. III.

Secondly, using the formulae derived in Sec. III as a starting point we provide in Sec. IV a wide range of results for the detector statistics of electro-optic sampling experiments of the quantum vacuum at different levels of approximation. These extend those derived in Ref. [18] by including effects of beam divergence, simplified analytical expressions for correlation measurements between distinct spatio-temporal regions using two laser pulses as in Ref. [10] as well as effects arising from non-parallel laser pulses. The variously approximated results are finally compared to the experimental data taken from Ref. [10]. The wide applicability of different approximated results and the discussion of the parameter ranges in which they apply as discussed in this paper offer a toolbox for analysis of future experiments accessing different characteristics of the quantum vacuum with high precision.

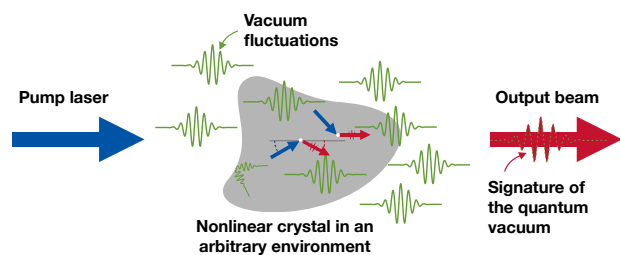


Figure 2. *Illustration of our theoretical framework.* A coherent pump pulse is incident on a nonlinear crystal in arbitrary environment. Inside the crystal the pump pulse can mix with the vacuum fluctuations via nonlinear processes as indicated by the arrows.

II. WAVE PROPAGATION THROUGH NONLINEAR MEDIA

In this section we recapitulate the theoretical formalism developed in Ref. [18] for predicting the quantised electric field behind a nonlinear crystal through which a coherent laser pulse propagates (see Fig. 2 for the general setup under consideration). This framework includes absorption, dispersion and additional macroscopic bodies surrounding the nonlinear crystal, meaning the full medium-assisted ground state is incorporated as described by macroscopic QED. We first review some basics of macroscopic QED in Sec. II A before applying it to propagation of a laser pulse through a non-linear crystal in Sec. II B. In Sec. II C a new diagrammatic representation of this result is introduced which will turn out to be a convenient way to deal with the in principle vast number of terms contributing to the operator for the electric field emerging from the crystal. This diagrammatic representation is applied to the setup of electro-optic sampling in Sec. III, but can be used in a wider context where light propagation through nonlinear absorptive media is considered.

A. Macroscopic QED

In order to obtain the quantised electro-magnetic field in media, one could exploit microscopic models such as that proposed by Huttner and Barnett [19]. This framework, however, relies on a specific material model under consideration. Here, we use the more general framework of macroscopic QED which can be obtained either phenomenologically (as was done in the original work [20]) or from canonical quantisation of classical macroscopic electrodynamics [17]. It relies on the knowledge of the relative linear permittivity ϵ and permeability μ of all materials involved, although in this paper we restrict ourselves to materials which do not have a magnetic response, i.e. $\mu = 1$. Note, however, that this is only for convenience and including magnetically responding media is straightforward [16]. When quantising the electromagnetic field in the presence of media one finds that its fundamental excitations are those of a joint field–matter system — so called *polaritonic* modes. In the following we

briefly recap the basic construction of the electric field operator and the state space as predicted by macroscopic QED, more detailed discussions of which can be found in Refs. [15, 16].

The polaritonic modes can be seen as being generated by a noise polarisation $\hat{\mathbf{P}}_{\text{N}}$, given by

$$\hat{\mathbf{P}}_{\text{N}}(\mathbf{r}, \omega) = i\sqrt{\frac{\hbar\epsilon_0}{\pi}} \text{Im}\epsilon(\mathbf{r}, \omega) \hat{\mathbf{f}}(\mathbf{r}, \omega). \quad (1)$$

Here $\hat{\mathbf{f}}(\mathbf{r}, \omega)$ and $\hat{\mathbf{f}}^\dagger(\mathbf{r}, \omega)$ are the bosonic annihilation and creation operators of the medium-assisted polaritonic modes and throughout we have

$$\hat{\mathbf{X}}(\mathbf{r}, t) = \int_0^\infty d\omega \hat{\mathbf{X}}(\mathbf{r}, \omega) e^{-i\omega t} + \text{h.c.} \quad (2)$$

Introducing this noise polarization into Maxwell's equations, one obtains finds that $\hat{\mathbf{P}}_{\text{N}}$ acts as a source term in the following inhomogeneous wave equation:

$$\left(\nabla \times \nabla \times - \frac{\omega^2}{c^2} \epsilon(\mathbf{r}, \omega) \right) \hat{\mathbf{E}}_{\text{vac}}(\mathbf{r}, \omega) = -\mu_0 \omega^2 \hat{\mathbf{P}}_{\text{N}}. \quad (3)$$

This can be solved by means of the classical Green's tensor \mathbf{G} , such that one finds the ground state field operator in media

$$\hat{\mathbf{E}}_{\text{vac}}(\mathbf{r}, \omega) = i\frac{\omega^2}{c^2} \sqrt{\frac{\hbar\epsilon_0}{\pi}} \times \int d^3r' \sqrt{\text{Im}\epsilon(\mathbf{r}', \omega)} \mathbf{G}(\mathbf{r}, \mathbf{r}', \omega) \cdot \hat{\mathbf{f}}(\mathbf{r}', \omega), \quad (4)$$

where \mathbf{G} is defined by

$$\left(\nabla \times \nabla \times - \frac{\omega^2}{c^2} \epsilon(\mathbf{r}, \omega) \right) \mathbf{G}(\mathbf{r}, \mathbf{r}', \omega) = \delta(\mathbf{r} - \mathbf{r}') \quad (5)$$

and the boundary condition $\mathbf{G}(\mathbf{r}, \mathbf{r}', \omega) \rightarrow 0$ for $|\mathbf{r} - \mathbf{r}'| \rightarrow \infty$. The Green's function can be viewed as a propagator for excitations of frequency ω emanating from a point-like dipole source at position \mathbf{r}' to an observation point \mathbf{r} . It is known in closed form for different geometries such as e.g. planar multilayer systems [21], cylindrical systems such as fibres [22] or systems which are spherically symmetric [23], with more complex geometries requiring approximation or numerical methods.

In order to be able to calculate expectation values, we construct the Hilbert space of the system as the Fock space generated by the polaritonic creation and annihilation operators. This polaritonic construction means that the states (including the ground state) can be altered by the presence of the media compared to their free space counterparts.

Since the polaritonic creation and annihilation operators follow bosonic statistics, one finds as expected that the vacuum electric field operator vanishes on average, i.e. $\langle \hat{\mathbf{E}}_{\text{vac}} \rangle = 0$. However, its two-point correlation function is in general different from zero:

$$\langle \hat{\mathbf{E}}(\mathbf{r}, \omega) \hat{\mathbf{E}}^\dagger(\mathbf{r}', \omega') \rangle = \frac{\hbar\mu_0}{\pi} \omega^2 \times \delta(\omega - \omega') [1 + 2n_{\text{T}}(\omega)] \text{Im}\mathbf{G}(\mathbf{r}, \mathbf{r}', \omega). \quad (6)$$

where $n_{\text{T}}(\omega)$ is the average thermal photon number at temperature T governed in thermal equilibrium by Bose–Einstein statistics [24, 25]

$$n_{\text{T}}(\omega) = \frac{1}{e^{\hbar\omega/(k_{\text{B}}T)} - 1} \quad (7)$$

where k_{B} is the Boltzmann constant. Note that n_{T} vanishes as $T \rightarrow 0$, so that the two terms in the factor $1 + 2n_{\text{T}}(\omega)$ in Eq. (6) represent vacuum and thermal fluctuations, respectively.

Equations (4) and (6) describe the statistics of quantised electromagnetic field fluctuations in media, their polaritonic nature accounting for the fields generated by the fluctuations of the charges in the medium. Note that the two-point correlation function (6) finds importance in many different physical processes (for a general overview see, e.g., [3, 16]) including Casimir [4] and Casimir–Polder forces [8], spontaneous decay [2], the Purcell effect [7] and resonant energy transfer [6, 26].

B. Wave equation and perturbative solution

Our schematic picture of the system is shown in Fig. 2 where a laser pulse propagates through a nonlinear crystal of arbitrary shape as first discussed in Ref. [18]. To this end, we introduce two additional sources into the wave equation Eq. (3), so that it reads

$$\left(\nabla \times \nabla \times - \frac{\omega^2}{c^2} \epsilon(\mathbf{r}, \omega) \right) \hat{\mathbf{E}}(\mathbf{r}, \omega) = -\mu_0 \omega^2 \left[\hat{\mathbf{P}}_{\text{NL}} + \mathbf{P}_{\text{p}} + \hat{\mathbf{P}}_{\text{N}} \right]. \quad (8)$$

The first of there is the nonlinear polarisation $\hat{\mathbf{P}}_{\text{NL}}$, which has been added to account for the nonlinear response of the crystal assumed to have the general form [27]

$$\hat{\mathbf{P}}_{\text{NL}}(\mathbf{r}, \omega) = \int_{-\infty}^{\infty} d\Omega \chi^{(2)}(\mathbf{r}, \omega - \Omega, \Omega) \star \hat{\mathbf{E}}(\mathbf{r}, \omega - \Omega) \hat{\mathbf{E}}(\mathbf{r}, \Omega). \quad (9)$$

Here, $\chi^{(2)}$ is the nonlinear susceptibility tensor of the electro-optical crystal and we have defined a shorthand

$$[\chi^{(2)} \star \hat{\mathbf{E}}\hat{\mathbf{E}}]_i \equiv \sum_{jk} \chi_{ijk}^{(2)} \hat{E}_j \hat{E}_k$$

The other source introduced in Eq. (8) is the coherent laser pulse. This results in an electric field \mathbf{E}_{p} which, in the vacuum picture [28], causes the total field to take the form $\hat{\mathbf{E}} = \hat{\mathbf{E}}_{\text{vac}} + \mathbf{E}_{\text{p}}$. The field \mathbf{E}_{p} is related to \mathbf{P}_{p} via

$$\mathbf{E}_{\text{p}}(\mathbf{r}, \omega) = -\mu_0 \omega^2 \int d^3r' \mathbf{G}(\mathbf{r}, \mathbf{r}', \omega) \cdot \mathbf{P}_{\text{p}}(\mathbf{r}', \omega), \quad (10)$$

see App. B for details. Note that $\mathbf{E}_{\text{p}}(\mathbf{r}, \omega)$ can represent any number of spatially and temporally separated

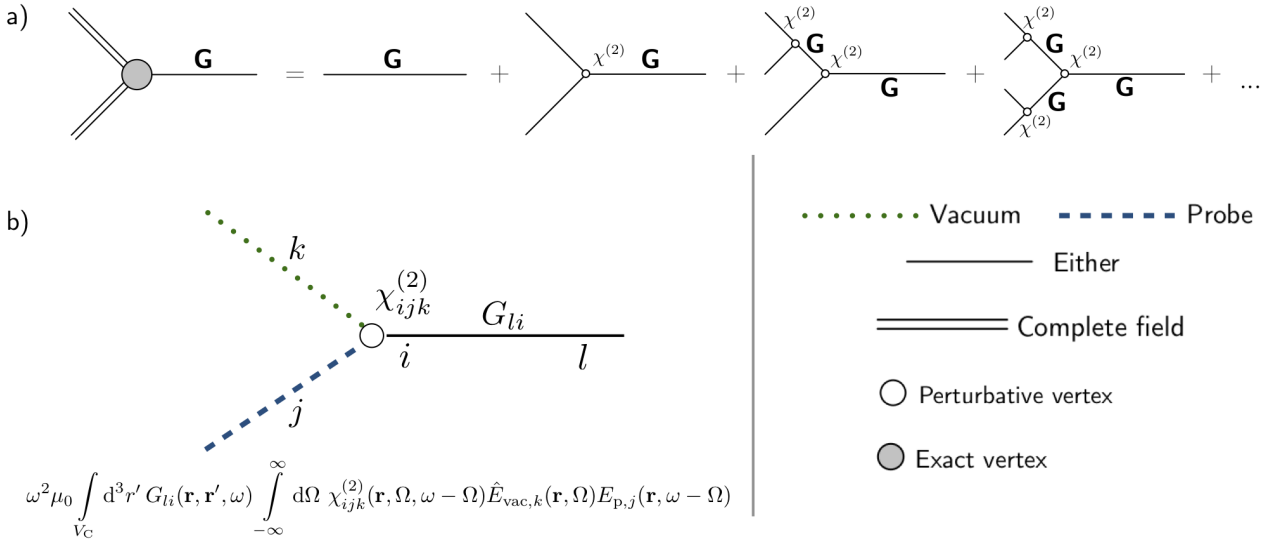


Figure 3. *Diagrammatic representation of the perturbative approach:* (a) The electric field emerging from the crystal is represented by an exact vertex found on the left hand side. Expanding the electric field in orders of $\chi^{(2)}$ as in Eqs. (14) and (15), this exact vertex can be expanded into perturbative vertices. In terms of formulae, (a) reads $\hat{\mathbf{E}} = \hat{\mathbf{E}}^{(0)} + \hat{\mathbf{E}}^{(1)} + \hat{\mathbf{E}}^{(2)} + \hat{\mathbf{E}}^{(3)} + \dots$ where only representative diagrams are shown here. If a more detailed discussion is needed, one can specify the polarisation of all fields involved as indicated in (b).

classical laser pulses. The wave equation (8) can formally be solved by a Lippmann-Schwinger equation

$$\hat{\mathbf{E}}(\mathbf{r}, \omega) = -\mu_0 \omega^2 \int d^3 r' \mathbf{G}(\mathbf{r}, \mathbf{r}', \omega) \cdot \left[\hat{\mathbf{P}}_{\text{NL}}(\mathbf{r}', \omega) + \mathbf{P}_p(\mathbf{r}', \omega) + \hat{\mathbf{P}}_N(\mathbf{r}', \omega) \right] \quad (11)$$

as can be seen by inserting Eq. (11) into Eq. (8). Upon recalling the definition of $\hat{\mathbf{E}}_{\text{vac}}$ in Eq. (4) one obtains from Eqs. (10) and (11)

$$\hat{\mathbf{E}}(\mathbf{r}, \omega) = \mathbf{E}_p(\mathbf{r}, \omega) + \hat{\mathbf{E}}_{\text{vac}}(\mathbf{r}, \omega) - \mu_0 \omega^2 \int_{V_C} d^3 r' \mathbf{G}(\mathbf{r}, \mathbf{r}', \omega) \cdot \hat{\mathbf{P}}_{\text{NL}}(\mathbf{r}', \omega). \quad (12)$$

Here, V_C is the volume of the crystal.

Equations (9) and (12) define a formal solution for $\hat{\mathbf{E}}(\mathbf{r}, \omega)$, but are infinitely recursive. To solve them, we follow Ref. [18] where a Born series is used, which can be seen as a perturbative expansion in the nonlinear susceptibility tensor $\chi^{(2)}$ to the desired order. To keep track of this order we introduce a scalar perturbation parameter α via $\chi^{(2)} \rightarrow \alpha \chi^{(2)}$, which will be set to unity at the end of the calculation. We expand the fields in orders of α ,

$$\hat{\mathbf{E}}(\mathbf{r}, \omega) = \sum_{i=0}^{\infty} \alpha^i \hat{\mathbf{E}}^{(i)}(\mathbf{r}, \omega), \quad (13)$$

which can then be inserted into Eq. (12). Comparing the terms of order α^i on the left and right hand side of the resulting expression, one finds for $i = 0$

$$\hat{\mathbf{E}}^{(0)}(\mathbf{r}, \omega) = \hat{\mathbf{E}}_{\text{vac}}(\mathbf{r}, \omega) + \mathbf{E}_p(\mathbf{r}, \omega), \quad (14)$$

and for $i > 0$

$$\hat{\mathbf{E}}^{(i)}(\mathbf{r}, \omega) = - \sum_{j=1}^i \mu_0 \omega^2 \int_{V_C} d^3 r' \mathbf{G}(\mathbf{r}, \mathbf{r}', \omega) \cdot \int_{-\infty}^{\infty} d\Omega \chi^{(2)}(\mathbf{r}', \omega - \Omega, \Omega) \star \hat{\mathbf{E}}^{(i-j)}(\mathbf{r}', \Omega) \hat{\mathbf{E}}^{(j-1)}(\mathbf{r}', \omega - \Omega). \quad (15)$$

Equations (14) and (15) describe the electric field operator emerging from a nonlinear crystal through which a coherent laser pulse with arbitrary profile propagates as dictated by the Helmholtz equation and the polaritonic environment. In particular, this result goes beyond the paraxial approximation. Furthermore, the realistic material response and the electromagnetic properties of the environment can be taken into account via the linear permittivity $\varepsilon(\mathbf{r}, \omega)$ which enters the Green's tensor.

This approach can be used in a variety of contexts such as spontaneous parametric down-conversion [29], generation of subcycle squeezed light [30, 31] or nonlinear effects in dispersion forces such as the Casimir force [32]. To make our theoretical formalism more amenable to these different applications, we introduce a diagrammatic way to represent the different terms in Eqs. (14) and (15) in the next section. This diagrammatic approach will turn out to be a convenient tool to understand and discuss their physical significance and to keep track of the vast number of terms in Eq. (15).

C. Diagrammatic approach

A diagrammatic representation of the perturbative solution of Eqs (11), [given by (14) and (15)] can be found in Fig. 3. The incoming fields, i.e. the laser and

the vacuum field, can either propagate freely through the crystal or interact with it, forming a three point vertex and picking up a factor of $\chi_{ijk}^{(2)}$ for incoming fields with polarization j, k and an outgoing field with polarisation i . The resulting field can subsequently form a new three-point vertex in the same way. This can happen multiple times, each new vertex representing an increase in the order of perturbation theory. Note that conservation of energy implies that the sum over all frequencies at each vertex equals zero.

Each diagram in Fig. 3 (a) represents a large number of different terms in the expansion, since every incoming line on the right hand side of Fig. 3 (a) can represent any of the (possible multiple) laser pulses or the vacuum field. Furthermore, we have not specified the directions into which the various fields are polarised. In order to evaluate the series, we therefore label each vertex and line with a polarization index and partition the whole series into diagrams where the incoming line represents the vacuum field, and those where it represents the probe field, as shown in Fig. 3 (b).

We demonstrate the utility of this diagrammatic approach in the following section in which we apply it to the setup of electro-optic sampling.

III. ELECTRO-OPTIC SAMPLING

In this section we apply the theoretical framework developed in the last section to the setup of electro-optic sampling following the method introduced in Ref. [18]. Here, we extend the discussion by including a diagrammatic description of the calculation as well as finding a new relation revealing how electro-optic sampling can retrieve the wave vector dependence of the two-point correlation function, cf. Eqs. (35) and (37). Also, we derive new equations for the signal as a function of the time delay and lateral shift between the two laser beams of the two-beam setup which, surprisingly, only depend on the single-beam filter function. We begin in Sec. III A by considering the single-beam setup as in Refs. [9, 33], whereas in Sec. III B we generalise these results to the what we call the two-beam setup that was realised in Ref. [10].

A. Single beam

We consider the basic experimental scheme depicted in Fig. 4, which has been discussed by various previous authors [9, 33]. The laser pulse is linearly polarised in the y direction and propagates in the z -direction; its transverse profile can be chosen arbitrarily. Furthermore, the nonlinear crystal is chosen to be a zincblende-type material with symmetry group $\bar{4}3m$, whose lattice vectors are orientated in the fol-

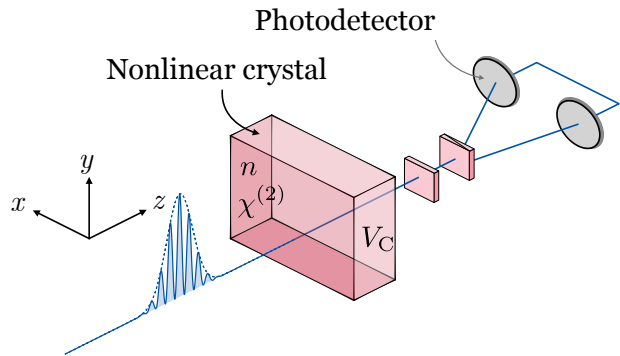


Figure 4. *Single-beam setup: Single-beam setup of electro-optic sampling:* One linearly polarised laser beam (blue) propagates through a nonlinear crystal with linear refractive index n , nonlinear susceptibility $\chi^{(2)}$ and volume V_C . The field emerging from the crystal is analysed by ellipsometry consisting of a $\lambda/4$ plate, a Wollaston prism and two balanced photodetectors. This is basic setup of electro-optic sampling [11, 12] which has been used this way in Ref. [9] to measure the quantum vacuum.

lowing way:

$$\begin{aligned} [100] &= \frac{1}{\sqrt{2}}(\mathbf{e}_z - \mathbf{e}_x), \\ [010] &= \frac{1}{\sqrt{2}}(\mathbf{e}_z + \mathbf{e}_x), \\ [001] &= \mathbf{e}_y, \end{aligned}$$

where \mathbf{e}_i is a unit vector in the i th direction. In this configuration the nonlinear polarisation in the laboratory frame is given by

$$\hat{\mathbf{P}}_{\text{NL}} = 2\chi^{(2)} \left[-\hat{E}_y \hat{E}_x \mathbf{e}_x + \hat{E}_y \hat{E}_z \mathbf{e}_z + \frac{1}{2} \left(\hat{E}_x^2 - \hat{E}_z^2 \right) \mathbf{e}_y \right] \quad (16)$$

where we have omitted the frequency and position arguments for brevity, but emphasise that we allow $\chi^{(2)}$ to be a frequency-dependent, complex quantity. The field emerging from the crystal is detected by an ellipsometry scheme resulting in a differential photocount whose expectation value \bar{m} and variance Δm can be found to be given by [18, 33]

$$\bar{m} = \langle : \hat{S} : \rangle, \quad (17)$$

$$(\Delta m)^2 = N + \langle : \hat{S}^2 : \rangle - \langle : \hat{S} : \rangle^2. \quad (18)$$

Here, $: \dots :$ denotes normal ordering and the electro-optic sampling operator is given by

$$\hat{S} = 4\pi\epsilon_0 c \int_0^\infty d\omega \frac{n(\omega)\eta(\omega)}{\hbar\omega} \times \int d^2 r_{\parallel} \left[i\hat{E}_y^\dagger(\mathbf{r}_{\parallel}, \omega) \hat{E}_x(\mathbf{r}_{\parallel}, \omega) + \text{h.c.} \right]. \quad (19)$$

The term N appearing on the right hand side of Eq. (18) is related to the total number of detected photons and is usually referred to as the shot noise.

In order to evaluate Eqs. (17) and (18) one has to find the electro-optical signal operator \hat{S} given by

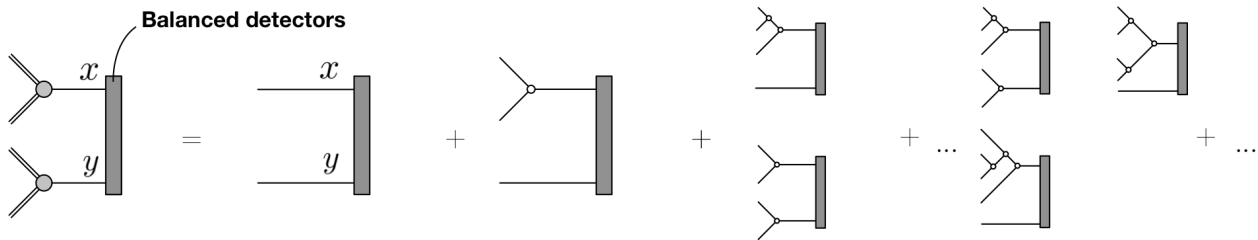


Figure 5. *Diagrams contributing to \hat{S}* : The electro-optical signal \hat{S} is quadratic in the electric field, so it is diagrammatically described by two exact vertices. Each of these can be expanded into perturbative vertices as before, c.f. Fig. 3.

Eq. (19), which is still written in terms of the (unknown) output field behind the crystal, rather than the (known) input field and crystal properties. In the remainder of this section we describe how the output field can be expressed in terms of known quantities by using the Born-series approach and its diagrammatic interpretation outlined in Secs. II B and II C. In all that follows, we restrict the perturbation series to second order in $\chi^{(2)}$.

We begin by considering contributions to $\langle : \hat{S} : \rangle$, which will give us the expectation value of the differential photocount and one term from its variance via Eqs. (17) and (18). Since $\langle : \hat{S} : \rangle$ is quadratic in the electric field operator we have to formally square the diagrams found in Fig. 3(a) as shown in Fig. 5. This gives numerous possible terms, many of which do not contribute. To demonstrate this we make use of four basic rules:

- (i) Only diagrams with an even number of vacuum fields contribute.
- (ii) Vacuum fields cannot be directly measured by the photomultipliers.
- (iii) Diagrams proportional to off-diagonal elements of \mathbf{G} do not contribute, i.e. the polarisation of a field does not change upon propagation.
- (iv) Vacuum fields with different polarisations are uncorrelated, i.e. $\langle \hat{E}_{\text{vac},i} \hat{E}_{\text{vac},j}^\dagger \rangle = 0$ if $i \neq j$.

Rule (i) follows from the linear dependence of $\hat{\mathbf{E}}_{\text{vac}}$ on the bosonic creation and annihilation operators [see Eq. (4)], while rule (ii) is a consequence of the normal ordering in Eqs. (17) and (18). Rule (iii) on the other hand can be shown to be true if the system exhibits inversion symmetry along the x and y axis and rule (iv) is a direct consequence of rule (iii) as can be seen from Eq. (6). Using rules (i)–(iv) (as well as verifying by explicit calculation) we find as anticipated that the expectation value of the signal vanishes:

$$\langle : \hat{S} : \rangle = 0, \quad (20)$$

which is a direct consequence of the fact that the ground state expectation value of $\hat{\mathbf{E}}_{\text{vac}}$ is zero.

Next, we evaluate the contribution to the signal's variance given by $\langle : \hat{S}^2 : \rangle$. Since $\langle : \hat{S}^2 : \rangle$ depends on the electric field to the fourth power, we have to square the diagrams in Fig. 5. By making use of the rules

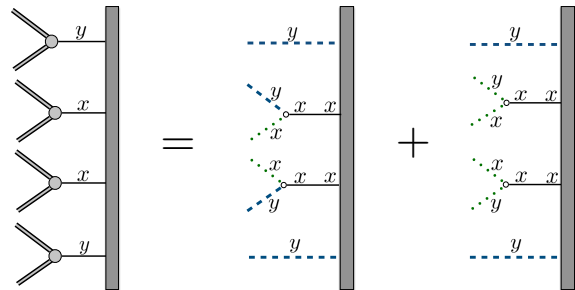


Figure 6. *Diagrams contributing to $\langle : \hat{S}^2 : \rangle$* : The squared electro-optical operator $\langle : \hat{S}^2 : \rangle$ is quartic in the fields such that one has to expand four exact vertices. Doing so by making use of rules (i)–(iv) one finds that only the two diagrams shown here are the ones which contribute to the signal.

(i)–(iv) we find up to second order in $\chi^{(2)}$ that the only diagrams contributing are those shown in Fig. 6. Since the vacuum field is much weaker than that of the laser pulse, we can neglect the diagram on the right hand side in Fig. 6. Translating the first diagram back to a formula, one obtains

$$\hat{S}^2 = \left[\int_{-\infty}^{\infty} d\Omega \int_{V_C} d^3r' \hat{E}_{\text{vac},x}(\mathbf{r}', \Omega) H(\mathbf{r}', \Omega) + \text{h.c.} \right]^2, \quad (21)$$

where

$$H(\mathbf{r}', \Omega) = -8\pi i c \varepsilon_0 \chi^{(2)}(\Omega) \mu_0 \int_0^{\infty} d\omega \frac{\eta(\omega) \sqrt{\varepsilon(\omega)} \omega}{\hbar} \times \int d^2r_{\parallel} E_{p,y}^*(\mathbf{r}_{\parallel}, \omega) \mathbf{G}_{xx}(\mathbf{r}_{\parallel}, \mathbf{r}', \omega) E_{p,y}(\mathbf{r}', \omega - \Omega). \quad (22)$$

Here we have assumed that $\chi^{(2)}$ is constant within the range of frequencies making up the laser pulse, such that it only depends on the frequency of the vacuum field Ω . Note generalising the formalism to a nonlinear susceptibility which also depends on the frequency of the laser pulse is straightforward.

To simplify Eq. (21) we follow Ref. [18] and use the reality relation $\hat{E}_{\text{vac},x}(\mathbf{r}', -\Omega) = \hat{E}_{\text{vac},x}^\dagger(\mathbf{r}', \Omega)$ to shift

to positive frequencies Ω only;

$$\hat{S}^2 = \left(\int_0^\infty d\Omega \int_{V_C} d^3r' \hat{E}_{\text{vac},x}(\mathbf{r}', \Omega) \times [H(\mathbf{r}', \Omega) + H^*(\mathbf{r}', -\Omega)] + \text{h.c.} \right)^2. \quad (23)$$

Using the commutation relations of the creation and annihilation operators, we see that the only term contributing is the one which depends on $\hat{E}_x \hat{E}_x^\dagger$ so that we find

$$\langle : \hat{S}^2 : \rangle = \int_0^\infty d\Omega \int_0^\infty d\Omega' \int_{V_C} d^3r' \int_{V_C} d^3r'' \times \langle \hat{E}_{\text{vac},x}(\mathbf{r}', \Omega) \hat{E}_{\text{vac},x}^\dagger(\mathbf{r}'', \Omega') \rangle F_1(\mathbf{r}', \mathbf{r}'', \Omega, \Omega'), \quad (24)$$

where

$$F_1(\mathbf{r}', \mathbf{r}'', \Omega, \Omega') = [H(\mathbf{r}', \Omega) + H^*(\mathbf{r}', -\Omega)] \times [H^*(\mathbf{r}'', \Omega') + H(\mathbf{r}'', -\Omega')]. \quad (25)$$

Lastly, we use macroscopic QED to evaluate the expectation value of the two-point correlation function of the electric field operator. This amounts to inserting Eq. (6) into Eq. (24), giving;

$$\langle : \hat{S}^2 : \rangle = \frac{\hbar\mu_0}{\pi} \int_0^\infty d\Omega \int_{V_C} d^3r' \int_{V_C} d^3r'' [1 + 2n_T(\Omega)] \times \Omega^2 \text{Im}[\mathbf{G}_{xx}(\mathbf{r}', \mathbf{r}'', \Omega)] F_1(\mathbf{r}', \mathbf{r}'', \Omega). \quad (26)$$

with $F_1(\mathbf{r}', \mathbf{r}'', \Omega) \equiv F_1(\mathbf{r}', \mathbf{r}'', \Omega, \Omega)$.

We see in Eqs. (24)–(26), that by analysing the signal of an electro-optic sampling experiment one can retrieve information about the two-point correlation function of the electromagnetic field, sampled within the spatio-temporal extent of the laser pulse. The latter is determined by the integration over the crystal volume and the function F_1 , which we henceforth refer to as a *filter* function, since it plays the role of singling out a particular spacetime region in which the vacuum field is observed — reminiscent of the role of the plates in the Casimir force. The advantage of this method over more traditional routes to the quantum vacuum is its versatility: which part of the correlation function is accessed in the experiment can be chosen by tuning the filter function. This can be done by varying relatively easily-accessed experimental parameters such as the pump beam profile and duration, which have no analogue in Casimir force experiments. Even more flexible and comprehensive access to the two-point correlation function is achieved with a slightly more elaborate experimental setup using two laser beams, discussed in the next section.

B. Generalisation to two beams

In more recent experiments, the setup shown in Fig. 7 has been extended to having two laser beams

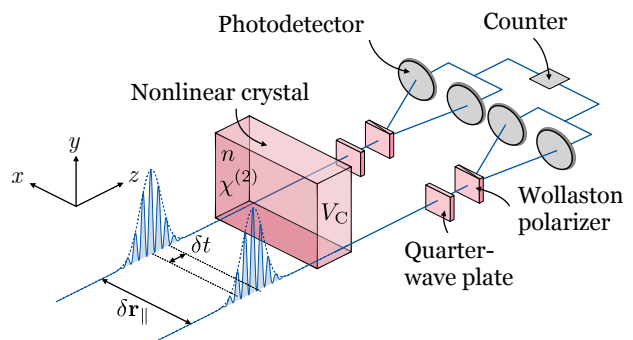


Figure 7. *Two-beam setup*: The two-beam setup consists of two identically-shaped, linearly polarised laser pulses with spatial offset $\delta\mathbf{r}_\parallel$ and relative time delay δt . They both propagate through a nonlinear crystal and are analysed separately after emerging from the crystal by the same ellipsometry also used for the single beam setup, compare Fig. 4. This setup has been used in Ref. [10] to measure the spectral decomposition of the electro-magnetic quantum vacuum.

(see Fig. 7), allowing for correlation measurements between different spatio-temporal regions [10]. It has been shown that this offers the significant advantage being able to experimentally access the *spectrum* of the electro-optic signal $s^2(\Omega)$, rather than just its integrated value $\langle : \hat{S}^2 : \rangle = \int_0^\infty d\Omega s^2(\Omega)$ [10]. In the following, we state the theoretical result found in Ref. [18] which can be seen as a generalisation of the theoretical framework outlined in the last section to the two-beam setup. We will further show a new relation which demonstrates, that this setup can be also used to not only access the spectral characteristics but also the wave-vector dependence of the polaritonic quantum vacuum fluctuations. We additionally derive simplified equations for the signal measured with arbitrary delays and spatial offsets between the laser pulses.

The main difference in the two-beam calculation compared to the single-beam case is the laser field. It is now given by two identically-shaped pulses with possible spatial offset in the lateral direction \mathbf{r}_\parallel and relative time delay δt such that the laser field is given by

$$\mathbf{E}_p(\mathbf{r}, t) = \mathbf{E}_1(\mathbf{r}, t) + \mathbf{E}_2(\mathbf{r}, t), \quad (27)$$

$$\mathbf{E}_1(\mathbf{r}, t) = \int_{-\infty}^{\infty} dt E(\mathbf{r}, \omega) e^{i\omega t} \mathbf{e}_y, \quad (28)$$

$$\begin{aligned} \mathbf{E}_2(\mathbf{r}, t) &= \int_{-\infty}^{\infty} dt E(\mathbf{r} + \delta\mathbf{r}, \omega) e^{i\omega\delta t} E_\delta(\mathbf{r}, \omega) e^{i\omega t} \mathbf{e}_y \\ &\equiv \int_{-\infty}^{\infty} dt E_\delta(\mathbf{r}, \omega) e^{i\omega t} \mathbf{e}_y. \end{aligned} \quad (29)$$

The Fourier transformed laser probe field is hence given by $E_p(\mathbf{r}, \omega) = E(\mathbf{r}, \omega) + E_\delta(\mathbf{r}, \omega)$ with $E_\delta(\mathbf{r}, \omega) \equiv E(\mathbf{r} + \delta\mathbf{r}, \omega) e^{i\omega\delta t}$.

Another less obvious difference compared to the single-beam calculation is given by the detection scheme. Since the two laser pulses are propagating into slightly different directions, they can be measured individually by two sets of balanced detectors, each of which consists of the same components as that described in Sec. III A. The statistics of this more general

setup reads [10, 18]

$$\bar{m} = \langle : \hat{S}(\delta\mathbf{r}, \delta t) : \rangle \quad (30)$$

$$\text{with } \hat{S}(\delta\mathbf{r}, \delta t) \equiv \frac{1}{2} \left\{ \hat{S}_1, \hat{S}_2 \right\}, \quad (31)$$

where $\{\cdot, \cdot\}$ denotes the anticommutator, and \hat{S}_i is the beam-specific electro-optic sampling operator, whose form in terms of electric fields is given by Eq. (19) with $\mathbf{E} \rightarrow \mathbf{E}_i$. Note that the diagram which contributes to $\langle : \hat{S}_1 \hat{S}_2 : \rangle$ is the same as in the previous section except that in the upper (lower) half of the diagram the laser pulse is given by \mathbf{E}_1 (\mathbf{E}_2). To find $\langle : \hat{S}_2 \hat{S}_1 : \rangle$ one simply replaces $\mathbf{E}_1 \leftrightarrow \mathbf{E}_2$. Translating this diagram back to formulae in the same way as was done for Eq. (21), we obtain up to second order in $\chi^{(2)}$ [18],

$$\begin{aligned} \langle : \hat{S}^2(\delta t, \delta\mathbf{r}_{\parallel}) : \rangle &= \int_0^{\infty} d\Omega \int_0^{\infty} d\Omega' \int_{V_C} d^3r' \int_{V_C} d^3r'' \\ &\times \langle E_{\text{vac},x}(\mathbf{r}', \Omega) E_{\text{vac},x}^{\dagger}(\mathbf{r}'', \Omega') \rangle F_{12}(\mathbf{r}', \mathbf{r}'', \Omega, \Omega'), \end{aligned} \quad (32)$$

with the generalized filter function for the two-beam setup;

$$\begin{aligned} F_{12}(\mathbf{r}, \mathbf{r}', \Omega, \Omega') &= \frac{1}{2} \left\{ [H_1(\mathbf{r}, \Omega) + H_1^*(\mathbf{r}, -\Omega)] \right. \\ &\times [H_2(\mathbf{r}', -\Omega') + H_2^*(\mathbf{r}', \Omega')] + [H_2(\mathbf{r}, \Omega) + H_2^*(\mathbf{r}, -\Omega)] \\ &\left. \times [H_1(\mathbf{r}', -\Omega') + H_1^*(\mathbf{r}', \Omega')] \right\} \end{aligned} \quad (33)$$

Equations (32) and (33) show that for the two-beam setup the two-point correlation function of the electric field's ground state is accessed in much the same way as for the single beam setup, but with a more general filter function F_{12} . For zero spatio-temporal offset ($\delta\mathbf{r}_{\parallel} = \delta t = 0$), F_{12} reduces to F_1 as can be seen from comparing their definitions in Eqs. (25) and (33). This also directly implies that $\langle : \hat{S}^2(0, \mathbf{0}) : \rangle = \langle : \hat{S}^2 : \rangle$.

The most important difference between the one- and two-beam filter functions is that the averaging of the two-point correlation function is over a single spatial region, while in the latter it is over regions which are in general distinct. This can be seen from the fact that $F_1(\mathbf{r}, \mathbf{r}') \propto E_{p,y}(\mathbf{r}) E_{p,y}(\mathbf{r}')$ while $F_{12}(\mathbf{r}, \mathbf{r}') \propto E_{1,y}(\mathbf{r}) E_{2,y}(\mathbf{r}')$. The connection between the single-beam and the two-beam setups can be made clearer by assuming that the crystal and the environment are invariant under shifts in the xy -plane by an arbitrary vector $\delta\mathbf{r}_{\parallel}$, i.e. $\mathbf{G}(\mathbf{r}, \mathbf{r}') = \mathbf{G}(\mathbf{r} \pm \delta\mathbf{r}_{\parallel}, \mathbf{r}' \pm \delta\mathbf{r}_{\parallel})$. This is true whenever we consider a crystal with lateral extension in the xy plane is much bigger than the beam waist of the laser pulses and their possible lateral offset, as will be done throughout the remainder of this work. Under this assumption it is straightforward to show that Eq. (32) can be rewritten as

$$\begin{aligned} \langle : \hat{S}^2(\delta t, \delta\mathbf{r}_{\parallel}) : \rangle &= \frac{1}{2} \int_0^{\infty} d\Omega \int_0^{\infty} d\Omega' \int_{V_C} d^3r' \int_{V_C} d^3r'' \\ &\times F_1(\mathbf{r}', \mathbf{r}'', \Omega) \left[\hat{E}_{\text{vac},x}(\mathbf{r}', \Omega) \hat{E}_{\text{vac},x}^{\dagger}(\mathbf{r}'' - \delta\mathbf{r}_{\parallel}, \Omega') e^{i\Omega'\delta t} \right. \\ &\left. + \hat{E}_{\text{vac},x}(\mathbf{r}' - \delta\mathbf{r}_{\parallel}, \Omega) \hat{E}_{\text{vac},x}^{\dagger}(\mathbf{r}'', \Omega') e^{-i\Omega'\delta t} \right], \end{aligned} \quad (34)$$

where F_1 is the *single-beam* filter function shown in Eq. (25), for the case where the one laser pulse which enters F_1 is given by \mathbf{E}_1 . Equivalently one can derive Eq. (34) with $\mathbf{E}_1 \rightarrow \mathbf{E}_2$ by replacing $\hat{E}_{\text{vac},x}^{\dagger}(\mathbf{r}'' - \delta\mathbf{r}_{\parallel}) \rightarrow \hat{E}_{\text{vac},x}^{\dagger}(\mathbf{r}'' + \delta\mathbf{r}_{\parallel})$ and $\hat{E}_{\text{vac},x}(\mathbf{r}' - \delta\mathbf{r}_{\parallel}) \rightarrow \hat{E}_{\text{vac},x}(\mathbf{r}' + \delta\mathbf{r}_{\parallel})$. Hence, we have rearranged the exponential factors introduced by the spatio-temporal shift of the second laser pulse in the two-beam measurement from the filter function to the two-point correlation function of the electric vacuum field. This way we obtained that the two-beam setup can equivalently be seen as sampling the two-point correlation function between two spatio-temporal regions which are shifted by $\delta\mathbf{r}_{\parallel}$ and δt relative to each other by means of the simplified one-beam filter function.

The introduction of a time delay between the pulses allows the spectrum of the signal to be accessed. To see this, we derive from Eqs (32) and (33) the relation

$$\begin{aligned} \frac{1}{8\pi^3} \int_{-\infty}^{\infty} d\delta t \int d^2\delta r_{\parallel} \langle : \hat{S}^2(\delta t, \delta\mathbf{r}_{\parallel}) : \rangle e^{i(\delta t\Omega + \mathbf{r}_{\parallel} \cdot \mathbf{q}_{\parallel})} \\ = \frac{1}{2} s^2(|\Omega|, \mathbf{q}_{\parallel}). \end{aligned} \quad (35)$$

Here, $s^2(\Omega, \mathbf{q}_{\parallel})$ is the signal obtained with the single beam setup decomposed into its dependence on the lateral wave vector and the frequency of the two-point correlation function, i.e.

$$\langle : \hat{S}^2 : \rangle = \int_0^{\infty} d\Omega \int d^2q_{\parallel} s^2(\Omega, \mathbf{q}_{\parallel}). \quad (36)$$

The explicit form of the integrand is;

$$\begin{aligned} s^2(\Omega, \mathbf{q}_{\parallel}) &\equiv \int_{V_C} d^3r' \int_{V_C} d^3r'' \frac{\hbar\mu_0}{\pi} \Omega^2 F_1(\mathbf{r}', \mathbf{r}'', \Omega, \Omega') \\ &\times \text{Im}[e^{i\mathbf{q}_{\parallel} \cdot (\mathbf{r} - \mathbf{r}')} \mathbf{G}_{xx}(z', z'', \mathbf{q}_{\parallel}, \Omega)], \end{aligned} \quad (37)$$

where $\mathbf{G}(z', z'', \mathbf{q}_{\parallel}, \Omega)$ is the $(2+1)$ -dimensional decomposition of the Green's tensor in Fourier space, i.e.

$$\mathbf{G}(\mathbf{r}, \mathbf{r}', \Omega) = \int d^2q_{\parallel} e^{i\mathbf{q}_{\parallel} \cdot (\mathbf{r} - \mathbf{r}')} \mathbf{G}(z, z', \mathbf{q}_{\parallel}, \Omega). \quad (38)$$

We emphasise this connection between the two-beam and one-beam setups: by measuring the electro-optic sampling operator of the *two-beam* setup for various time delays and spatial offsets, one is able to access the integrand of the electro-optic sampling observable of the *one-beam* setup $s^2(\Omega, \mathbf{q}_{\parallel})$ via Eq. (35). This means for the one-beam setup only the integrated, single-valued quantity $\langle : \hat{S}^2 : \rangle$ is obtained. This is similar to the Casimir force where also a wide range of frequencies contribute to one single observable. By contrast, the two-beam setup is able to resolve the spectrum of the vacuum two-point correlation function and its dependence on the lateral wave vector. This results in a uniquely versatile method of accessing the QED ground state in media. On a technical level this often yields the simplification that one only needs to model $s^2(\Omega, \mathbf{q}_{\parallel})$ which

can then be compared to experimental data. In other cases, however, one is not only interested in $s^2(\Omega, \mathbf{q}_{\parallel})$ but rather in the signal as a function of the lateral and temporal shift $\langle : \hat{S}^2(\delta t, \delta \mathbf{r}_{\parallel}) : \rangle$. Using a few general assumptions one is able to exploit Eq. (34) to find simplified expression for $\langle : \hat{S}^2(\delta t, \delta \mathbf{r}_{\parallel}) : \rangle$. Assuming that the crystal is isotropic and that reflection effects can be neglected, the xx -component of the imaginary part of the Green's tensor is given by (see Appendix A):

$$\text{Im}[G(\mathbf{r}', \mathbf{r}'', \Omega)] = \frac{1}{8\pi} \int_0^\infty dq_{\parallel} \int_0^{2\pi} d\phi q_{\parallel} e^{i\mathbf{q}_{\parallel} \cdot (\mathbf{r}' - \mathbf{r}'')} \times \text{Re} \left[\left(1 - \frac{q_x^2}{q^2} \right) \frac{e^{iq_z(z' - z'')}}{q_z} \right]. \quad (39)$$

Here, we have introduced polar coordinates for the lateral wave vector, i.e. $q_x = q_{\parallel} \sin(\phi)$ and $q_y = q_{\parallel} \cos(\phi)$. Next, we assume that the two laser pulses have a symmetric lateral profile which is smaller than the crystal surface, such that

$$\int_{V_C} d^3 r' \int_{V_C} d^3 r'' F_1(\mathbf{r}', \mathbf{r}'', \Omega, \Omega') e^{i\mathbf{q}_{\parallel} \cdot (\mathbf{r}' - \mathbf{r}'')}, \quad (40)$$

is independent of the angle ϕ . Using these results, one can use Eqs. (34) and (39) to show

$$\langle : \hat{S}^2(\delta t, \delta \mathbf{r}_{\parallel}) : \rangle = \int_0^\infty d\Omega \int_0^\infty dq_{\parallel} \cos(\Omega \delta t) s^2(\Omega, \delta \mathbf{r}_{\parallel}), \quad (41)$$

with

$$s^2(\Omega, \delta \mathbf{r}_{\parallel}) = \int_0^\infty dq_{\parallel} \int_{V_C} d^3 r' \int_{V_C} d^3 r'' \frac{\hbar \mu_0}{\pi} \Omega^2 F_1(\mathbf{r}', \mathbf{r}'', \Omega) \times \text{Re} \left[g(q_{\parallel}, \delta \mathbf{r}_{\parallel}) \frac{G_{xx}(z'z'', \mathbf{q}_{\parallel}, \Omega)}{1 - q_x^2/q^2} \right], \quad (42)$$

and

$$\frac{g(q_{\parallel}, \delta \mathbf{r}_{\parallel})}{2\pi} = \frac{1}{2\pi} \int_0^{2\pi} d\phi \left(1 - \frac{q_x^2}{q^2} \right) e^{i\mathbf{q}_{\parallel} \cdot \delta \mathbf{r}_{\parallel}} = \begin{cases} J_0(\delta x q_x) = -\frac{q_{\parallel}^2}{q^2} \left[\frac{J_1(\delta x q_x)}{\delta x q_x} - J_2(\delta x q_x) \right] & \text{if } \delta y = 0 \\ J_0(\delta y q_y) - \frac{q_{\parallel}^2}{q^2} \frac{J_1(\delta y q_y)}{\delta y q_y} & \text{if } \delta x = 0 \end{cases} \quad (43)$$

where J_n denotes the Bessel function of the first kind. Equations (41)-(43) represent a simpler way to obtain $\langle : \hat{S}^2(\delta t, \delta \mathbf{r}_{\parallel}) : \rangle$ compared to Eqs. (32) and (33) under the assumptions given above. They will be used in Sec. IV, where they are also compared to experimental data in Sec. IV D.

IV. RESULTS

In the last section we obtained formulae (24) and (32) which describe the statistics of electro-optic sampling experiments accounting for absorption, dispersion and general optical environments. In this section we exploit these in realistic contexts, initially, in

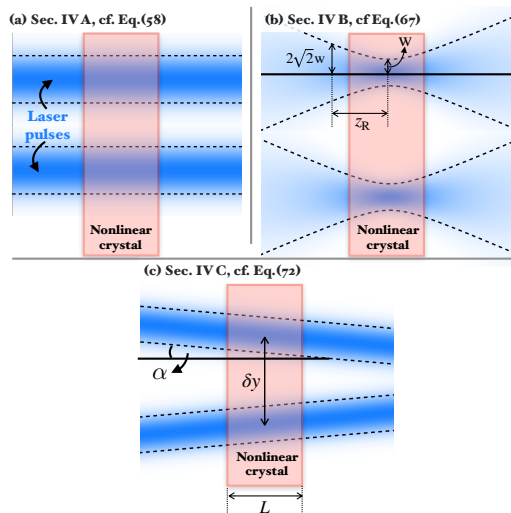


Figure 8. *Different levels of approximation:* (a) In Sec. IV A laser pulses with a constant Gaussian lateral beam profile are considered. (b) In Sec. IV B the divergence of the laser pulses is taken into account and (c) in Sec. IV C effects emerging from the fact that the two beams are propagating into slightly different direction are incorporated. In (a)-(c) also the main equation is referenced which can be used to calculate the electro-optic signal for the given setup under consideration.

Sec. IV A, by assuming a Gaussian pump-pulse profile, see Fig. 8 (a). For this setup we derive simplified equations for the variance of the detected signal using different approximations. This was similarly done in Ref. [18], but here we extend the discussion of the parameter range in which the different approximated results are valid.

In Secs. IV B and IV C we discuss, respectively, the influence onto the statistics of electro-optic sampling of the divergence of the laser pulses and of the fact that in the two-beam setup the two laser pulses are propagating into slightly different directions, see Fig. 8 (b) and (d). This allows one to study in which parameter range these effects have to be taken into account and in which particular way the signal is influenced by them. Additionally, by varying the beam width while keeping all other parameters constant, we obtain different regimes in which evanescent or propagating modes dominate the signal. The results derived in Secs. IV A-IV C offer a whole range of different approximated results and a discussion of the parameter ranges in which they apply and are best suited. This offers a convenient toolbox for future experiments measuring the quantum vacuum using electro-optic sampling.

Finally, in Sec. IV D, we compare the results coming out of our theoretical formalism discussed in Secs. IV A-IV C to experimental data.

A. Gaussian beams — different approximations

We assume that the crystal has length L and is centered at $z = 0$. Furthermore, we assume that its extension in the xy plane is infinite, which is a valid

approximation as long as the lateral extent of the crystal is much greater than that of the profile of the focused pump pulse in xy direction. The pump pulse is assumed to be given by a lowest order Laguerre-Gaussian mode

$$\mathbf{E}_p(\mathbf{r}, \omega) = E_p(\omega) \sqrt{\frac{2}{\pi w^2}} e^{-r_{\parallel}^2/w^2} e^{ikz} \mathbf{e}_y, \quad (44)$$

where w is the beam waist, $k = n(\omega)\omega/c$ is the wave vector of the laser pulse, $E_p(\omega)$ is its amplitude which also defines its spectral decomposition, and \parallel denotes the xy direction, i.e. $\mathbf{r}_{\parallel} = (x, y)^T$. Note that we have assumed that the Rayleigh length is much shorter than the length of the crystal, i.e. $w^2 k/2 \gg L$ in order to obtain the simplified expression of the lowest order Laguerre-Gaussian in Eq. (44). For the more general case in which $w^2 k/2 \gg L$ is not assumed, see Sec. IV B.

Neglecting reflection effects from the crystal's surfaces, but without applying any further approximations, one can evaluate Eq. (25) by inserting Eq. (44) and the bulk Green's tensor given by (A1), finding the filter function for the one-beam setup as derived in Ref. [18]

$$\begin{aligned} F(\mathbf{r}, \mathbf{r}', \Omega) &= \frac{16|\chi^{(2)}(\Omega)|^2}{\pi^2 c^2} \int_0^\infty d\omega \int_0^\infty d\tilde{\omega} \int d^2 k_{\parallel} \\ &\times \int d^2 \tilde{k}_{\parallel} \frac{n(\omega)\eta(\omega)\omega n(\tilde{\omega})\eta(\tilde{\omega})\tilde{\omega}}{\hbar^2} \left(1 - \frac{k_x^2}{k^2}\right) \left(1 - \frac{\tilde{k}_x^2}{\tilde{k}^2}\right) \\ &\times e^{-(r_{\parallel}^2 + r_{\parallel}'^2)/w^2} e^{-(k_{\parallel}^2 + \tilde{k}_{\parallel}^2)w^2/4 - i\mathbf{k}_{\parallel} \cdot \mathbf{r} + i\tilde{\mathbf{k}}_{\parallel} \cdot \mathbf{r}'} \\ &\times \text{Re}_{\Omega} \left[E_p^*(\omega) E_p(\omega - \Omega) \frac{e^{i[k_{\omega-\Omega} - k_z]z}}{k_z} \right] \\ &\times \text{Re}_{\Omega} \left[E_p^*(\tilde{\omega}) E_p(\tilde{\omega} + \Omega) \frac{e^{i[k_{\tilde{\omega}+\Omega} - \tilde{k}_z]z'}}{\tilde{k}_z} \right] \end{aligned} \quad (45)$$

where $\tilde{k} = n(\tilde{\omega})\tilde{\omega}/c$ and we defined a modified real part as

$$\text{Re}_{\Omega}[z(\Omega)] = \frac{1}{2}[z(\Omega) + z^*(-\Omega)]. \quad (46)$$

Inserting Eq. (45) into Eq. (24) one could obtain the signal without further approximation. The resulting formulae are very cumbersome so are not shown explicitly here, but can be significantly simplified by making some assumptions.

No absorption: We begin by neglecting absorption, assuming that the refractive index n is real in all frequency ranges involved. Using this approximation one obtains by inserting Eq. (45) into Eq. (24):

$$\begin{aligned} \langle : \hat{S}^2 : \rangle &= \frac{\hbar\mu_0 w^4 L^2}{\pi^3 c^2} \int_0^\infty d\Omega |\chi^{(2)}(\Omega)|^2 \Omega^2 \int_{q_{\parallel} < q} d^2 q_{\parallel} \\ &\times \left(1 - \frac{q_x^2}{q^2}\right) \frac{e^{-q_{\parallel}^2 w^2/2}}{q_z} \left| \int_0^\infty d\omega \int d^2 k_{\parallel} \right. \\ &\times \frac{n(\omega)\eta(\omega)\omega}{\hbar^2} \left(1 - \frac{k_x^2}{k^2}\right) e^{-(k_{\parallel}^2 + \mathbf{q}_{\parallel} \cdot \mathbf{k}_{\parallel})\frac{w^2}{2}} \\ &\times \text{Re}_{\Omega} \left[E_p^*(\omega) E_p(\omega - \Omega) \frac{\text{sinc}[\frac{L}{2}\Delta K_-]}{k_z} \right] \Big|^2 \\ &+ (\Delta K_- \rightarrow \Delta K_+). \end{aligned} \quad (47)$$

where we used the shorthand $\Delta K_{\pm} = k_{\omega-\Omega} - k_z \mp q_z$, and $+(\Delta K_- \rightarrow \Delta K_+)$ denotes adding the preceding term subject to the replacement $\Delta K_- \rightarrow \Delta K_+$. We see in Eq. (47) that due to the fact that we neglect absorption it is found that only propagating vacuum fields contribute to the signal whereas there is no contribution from evanescent ones. This can be seen from the fact that \mathbf{q}_{\parallel} is only integrated over a circle with radius q , instead of over all two-dimensional space. Note that to derive this result no additional assumptions were needed but it is found to be a consequence of neglecting absorption effects alone.

Equation (47) can be used as a starting point for further approximations, see also Ref. [18]. We begin by paraxially approximating the field generated by the nonlinear mixing in the frequency range of the laser by assuming that

$$n^2(\omega) \frac{\omega^2}{c^2} \gg \frac{1}{w^2} \quad \text{for } \omega \in [\omega_c - \Delta\omega, \omega_c + \Delta\omega]. \quad (48)$$

Here, ω_c and $\Delta\omega$ are the central frequency and the width of the spectrum of the laser pulse, respectively. We refer to Eq. (48) as the laser-paraxial approximation, since it implies that all fields whose frequencies belong to those sampled by the laser copropagate with it (i.e. in the z direction only). Furthermore, in the laser-paraxial approximation we also assume that within the frequency range of the laser we can assume a linear dependence of the refractive index on frequency by approximating [27]

$$k_{\omega-\Omega} - k_{\omega} \simeq -n_g \Omega/c, \quad (49)$$

where $n_g = c\partial k/\partial\omega|_{\omega=\omega_c}$ is the group refractive index at the central frequency of the laser pulse ω_c . This means we assume that there are no material resonance with frequencies close to the frequency range of the laser pulse. Using Eqs. (48) and (49) one obtains the filter function in the laser-paraxial approximation F_{LP} from Eq. (45) as [18];

$$\begin{aligned} F_{\text{LP}}(\mathbf{r}', \mathbf{r}'', \Omega) &= \left(\frac{4|\chi^{(2)}(\Omega)|c\mu_0 N\omega_p}{w^2 n(\omega_c)} \right)^2 f(\Omega)^2 \\ &\times e^{-2(\mathbf{r}_{\parallel}'^2 + \mathbf{r}_{\parallel}''^2)/w^2} e^{-in_g \frac{\Omega}{c}(z' - z'')}. \end{aligned} \quad (50)$$

Here, following Refs. [18, 33] we have introduced the average detected frequency

$$\omega_p = \frac{\int_0^\infty d\omega \eta(\omega) E_p(\omega)^2}{\int_0^\infty d\omega \frac{\eta(\omega)}{w} E_p(\omega)^2}, \quad (51)$$

and the spectral auto-correlation function

$$f(\Omega) = \frac{\int_0^\infty d\omega [E_p(\omega) E_p(\omega + \Omega) + E_p(\omega) E_p(\omega - \Omega)]}{2 \int_0^\infty d\omega \eta(\omega) E_p(\omega)^2}. \quad (52)$$

Inserting Eq. (50) into Eq. (26) we obtain the spectrum of the variance of the electro-optical signal in

the laser-paraxial approximation

$$s^2(\Omega) = \frac{(NL\omega_p)^2 \hbar |\chi^{(2)}(\Omega)|^2}{4\pi^3 c^4 \varepsilon_0^3 n^2(\omega_c)} \Omega^2 f(\Omega)^2 \int_{q_{\parallel} \leq q} d^2 q_{\parallel} \frac{1 - \frac{q_z^2}{q^2}}{q_z} \times e^{-q_{\parallel}^2 w^2/4} \left(\text{sinc} \left[\frac{L}{2} \Delta k_- \right]^2 + \text{sinc} \left[\frac{L}{2} \Delta k_+ \right]^2 \right) \quad (53)$$

where $\Delta k_{\pm} = n_g \frac{\Omega}{c} \pm q_z$ with $q_z = \sqrt{q^2 - q_{\parallel}^2}$, with $q = n(\Omega)\Omega/c$ being the wave vector at the frequency of the vacuum Ω .

We can also paraxially approximate the vacuum field by assuming

$$q^2 = n^2(\Omega) \frac{\Omega^2}{c^2} \gg \frac{1}{w^2}. \quad (54)$$

Since the exponential in Eq. (53) effectively restricts $q_{\parallel} < 2/w$, we find that Eq. (54) implies $q_{\parallel} \ll q$. This allows one to make use of the assumption shown in Eq. (54) by Taylor expanding Eq. (53) in orders of q_{\parallel}/q up to the first non-vanishing, post-paraxial order, i.e. third order in q_{\parallel}/q . Subsequently, one can carry out the \mathbf{q}_{\parallel} integral analytically, leading to

$$s^2(\Omega) = \frac{(NL\omega_p)^2 \hbar}{\pi^2 \varepsilon_0^3 c^3 n^3(\omega_c) w^2} \frac{n(\omega_c)}{n(\Omega)} |\chi^{(2)}(\Omega)|^2 \Omega f(\Omega)^2 \times \left\{ \left(1 - e^{-q^2 w^2/4} \right) \text{sinc} \left[\frac{L}{2} \Delta k_- \right]^2 + \left[\frac{4 - e^{-q^2 \omega_0^2/4} (4 + q^2 \omega_0^2)}{q \omega_0^2 \Delta k_-^2} \left(\text{sinc} [L \Delta k_-] - \text{sinc} \left[\frac{L}{2} \Delta k_- \right]^2 \right) \right] \right\} + (\Delta k_- \rightarrow \Delta k_+) \quad (55)$$

which we refer to as the Taylor-expanded result. Here $+(\Delta k_- \rightarrow \Delta k_+)$ denotes addition of the preceding term subject to the replacement $\Delta k_- \rightarrow \Delta k_+$. Note that here we have $\Delta k_{\pm} = n_g \frac{\Omega}{c} \pm q$. To further simplify the expression we can also restrict the Taylor expansion in Eq. (53) to its lowest order:

$$s^2(\Omega) = \frac{(NL\omega_p)^2 \hbar}{\pi^2 \varepsilon_0^3 c^3 n^3(\omega_c) w^2} \frac{n(\omega_c)}{n(\Omega)} |\chi^{(2)}(\Omega)|^2 \Omega f(\Omega)^2 \times \left(\text{sinc} \left[\frac{L}{2} \Delta k_- \right]^2 + \text{sinc} \left[\frac{L}{2} \Delta k_+ \right]^2 \right). \quad (56)$$

The first term of this expression coincides with the result obtained in Ref. [33], so that this more general approach reproduces the exact same results as the more specialised theory of Ref. [33] in the relevant limiting case [no absorption or reflection effects, wave vectors obeying Eqs. (48), (49) and (54)].

A few remarks concerning the structure of the different approximated results in Eqs. (47), (53), (55) and (56) are in order. First we see that in all of them the \mathbf{q}_{\parallel} integral is restricted by q which leads to $q_z \in \mathbb{R}$ since $n(\Omega) \in \mathbb{R}$. This means whenever absorption can be neglected, only propagating, transverse vacuum field fluctuations contribute. Note that

this is not true for general absorbing crystals as is discussed below and in Ref. [18]. Furthermore, in all of the approximated results we find two terms containing sinc-functions with arguments proportional to either Δk_+ or Δk_- [ΔK_+ or ΔK_- in Eq. (47)], accounting for phase-matching. The difference between Δk_+ and Δk_- [ΔK_+ or ΔK_- in Eq. (47)] is that in the former the wave vector of the vacuum modes is in the opposite direction to that of the laser field. Since this, in general, leads to reduced phase matching (at least for propagating waves) we call these terms off-resonant, and numerical evaluation shows that they are usually negligibly small. As is shown in Ref. [18] this is *not* true whenever the light-matter coupling is strong, i.e. when absorption is not negligible.

The spectral auto-correlation function defined in Eq. (52) demonstrates that it is crucial to use ultra-short laser pulses. One finds that the only frequencies contributing from the vacuum are those smaller than half of the spectral width of the laser pulse, such that the overlap of $E_p(\omega)$ and $E_p(\omega \pm \Omega)$ does not vanish. Physically, this can be understood by realising that only vacuum fluctuations whose wave length is longer than the spatial extensions of the laser pulse are resolved.

To summarize this section, we stated four different expressions for the spectrum of the electro-optical signal at four different levels of approximations: the full result in Eq. (47) where we only neglected absorption and reflections from the crystal surfaces, the laser paraxial approximated result in Eq. (53) where we additionally assumed Eqs. (48) and (49) to hold, and two different stages of the full-paraxial approximation found in Eqs (55) and (56) where we also applied the paraxial approximation to the vacuum fluctuations.

We now compare those approximations by evaluating the signal as a function of the beam waist, i.e. $\langle : S^2(\mathbf{w}) : \rangle$. To do so we fix all other parameters to those also used in Ref. [33] which are chosen in close analogy to the experimental realization in Ref. [9], i.e we set $l = 7 \mu\text{m}$ and we define the normalised spectrum of the laser pulse $E_p(\omega)$ to have a rectangular shape such that it is equal to one for $\omega \in [\omega_c - \Delta\omega, \omega_c + \Delta\omega]$ and zero otherwise. Choosing $\omega_c = 255 \times 2\pi$ THz and $\Delta\omega = 75 \times 2\pi$ THz leads to a pulse duration of $\Delta t = 5.9$ fs. The crystal is assumed to be made of ZnTe, such that the refractive index in the near-infrared frequency range is given by [36]

$$n(\omega)^2 = A + \left(\frac{B\lambda^2}{\lambda^2 - C} \right), \quad (57)$$

where $\lambda = 2\pi c/\omega$, $A = 4.27$, $B = 3.01$ and $C = 0.142$ leading to $n_g = 2.24$. In the THz frequency range we use [37]:

$$n(\Omega) = \text{Re} \left[\sqrt{\varepsilon_{\infty} \left(1 + \frac{(\hbar\omega_{\text{LO}})^2 - (\hbar\omega_{\text{TO}})^2}{(\hbar\omega_{\text{TO}})^2 - (\hbar\Omega)^2 - i\hbar\gamma\Omega} \right)} \right], \quad (58)$$

with $\omega_{\text{TO}} = 5.31 \times 2\pi$ THz, $\omega_{\text{LO}} = 6.18 \times 2\pi$ THz, $\gamma = 0.09 \times 2\pi$ THz and $\varepsilon_{\infty} = 6.7$. Neglecting the imaginary part in Eq. (58) is only valid as long as the

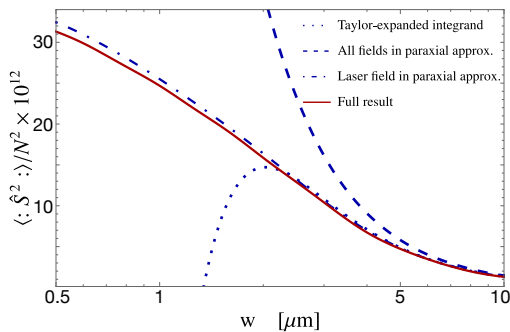


Figure 9. *Comparison of the different approximated results I:* We numerically evaluate $\langle : S^2(w) : \rangle$ as functions of the beam waist w using the different approximated results: The full-paraxial approximation (56), the result with a Taylor-expanded integrand (55), the laser paraxial one (53) and the full result (47).

frequencies under consideration are far from the material resonance which lies at approximately $40 \times 2\pi$ THz. The nonlinear susceptibility is given by $\chi^{(2)} = 1.17 \times 10^{-21} \text{ CV}^{-2}$ [37] and is assumed to be constant in the frequency range under consideration.

Using these definition we numerically evaluate $\langle : S^2(w) : \rangle$ and the result is plotted in Fig. 9. We find that for all values of w we have good agreement between the partial-paraxial and the full result. This is expected since Eqs. (48) and (49) are satisfied for all values of w shown in Fig. 9. Furthermore, for the parameters considered here it is mainly frequencies around $\Omega = 200 \times 2\pi$ THz that are accessed [18], such that according to Eq. (54) the paraxial approximation is only valid if $w \gg 0.5 \mu\text{m}$. This is confirmed in Fig. 9 where we see that only for $w > 2 \mu\text{m}$ the Taylor-expanded result offers a good approximate value, and the full paraxial approximated result starts to deviate from the full result already for values of the beam waist smaller than $5 \mu\text{m}$.

With absorption Next we also calculate the signal without neglecting absorption. Again one can find different stages of approximation by applying the paraxial approximation to the laser field and the vacuum field, respectively. As discussed in the previous paragraph, the laser paraxial approximation gives a reasonable level of agreement in experimentally feasible parameter regimes. Hence, when including absorption effects we only discuss the signal's spectrum in the laser paraxial approximation. This can be obtained by inserting Eq. (50) into Eq. (24) and allowing $n(\Omega)$ to be a complex quantity. Some algebra shows that in

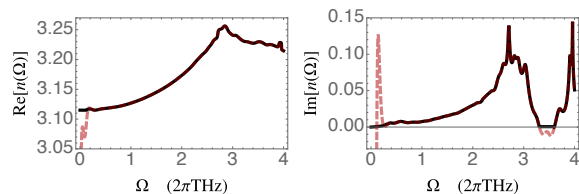


Figure 10. *Real and imaginary parts of the refractive index:* We show the real (left hand side) and imaginary part (right hand side) of the refractive index as measured in Ref. [10] at temperature $T = 4\text{K}$ (red dashed lines). The imaginary part is obtained from the measurement of the absorption coefficient α via $\alpha(\Omega) = \text{Im}[n(\Omega)]\Omega/c$. The real and imaginary parts used in the simulation is shown by the black solid lines and differ from the measured data only for very small frequencies $\Omega < 0.03 \times 2\pi$ THz in which the measurement apparently seems to give unreasonable results and in regions where $\text{Im}[n(\Omega)] < 0$ which violates causality and which would lead to diverging outcomes of the simulations.

this case (see also Ref. [18])

$$s^2(\Omega) = \hbar \frac{\left(N\omega_p \Omega f(\Omega) |\chi^{(2)}(\Omega)| \right)^2 [2n_T(\Omega) + 1]}{2\pi^2 c^4 \epsilon_0^3 n^2} \times \int_0^\infty dq_{\parallel} q_{\parallel} e^{-q_{\parallel}^2 w^2/4} \text{Re} \left[\left(2 - \frac{q_{\parallel}^2}{q^2} \right) \left(\frac{-iL}{q_z(n_g \Omega/c - q_z)} + \frac{1 - e^{iL(q_z - n_g \Omega/c)}}{q_z(q_z - n_g \Omega/c)^2} \right) + (n_g \rightarrow -n_g) \right]. \quad (59)$$

In Ref. [18] Eq. (59) was used to show that in case the resolved frequency range of the polaritonic vacuum fluctuations coincides with a material resonance for which $\text{Im}[\Omega]$ has a sharp peak, also the signal increases significantly due to longitudinal (so-called *matter-dominated*) fluctuations. Here, we show that even *far* from material resonances where $\text{Im}[\Omega]$ does not show any sharp peaks (but is only slightly bigger than zero) absorption must be taken into account in order to predict the electro-optic sampling signal. To do so, we consider the frequency range of the quantum-vacuum fluctuations accessed in Ref. [10] which is $\Omega \in [0, 4 \times 2\pi \text{ THz}]$. In order to avoid measuring thermal fluctuations we assume a temperature of $T = 4\text{K}$ as in the experiment [10] (see Sec. IV D for a discussion of the influence of thermal fluctuations). Furthermore we choose $L = 3\text{mm}$,

$$\mathbf{E}_p(\omega) = \sqrt{\frac{1}{\sigma}} \frac{e^{-(\omega - \omega_c)^2/\sigma^2}}{(2\pi)^{1/4}}, \quad (60)$$

with $\omega_c = 375 \times (2\pi) \text{ THz}$, $\sigma = \sqrt{2/\pi}(\Delta t)^{-1}$ and the pulse duration is given by $\Delta t = 80\text{fs}$. For the group refractive index in the near-infrared (frequency range of the laser) we use $n_g = 3.20$ which means we reduce the value measured at room temperature [compare Eq. (57)] since we assume $T = 4\text{K}$ [10]. For the nonlinear susceptibility we use [37]

$$\chi^{(2)}(\Omega) = \frac{n^4(\omega_C)\epsilon_0}{2} r_{41} \left[1 + C_0 \frac{(\hbar\omega_{\text{TO}})^2}{\hbar\Omega - i\hbar\Omega\gamma} \right], \quad (61)$$

Laser pulse (44)	with $\mathbf{E}_p(\omega) = \sqrt{\frac{1}{\sigma}} \frac{e^{-(\omega-\omega_c)^2/\sigma^2}}{(2\pi)^{1/4}}$, $\omega_c = 375 \times (2\pi)$ THz, $w = 125 \mu\text{m}$, $\sigma = \sqrt{2/\pi}(\Delta t)^{-1}$
group refractive index in near-infrared	$n_g = 3.20$
Refractive index	interpolation curves in Fig. 10
Temperature	$T = 4\text{K}$
Nonlinear susceptibility	Eq. (61) [37]
Length of crystal	$L = 3\text{mm}$

Table I. Parameters of the crystal and the laser pulse as in Ref. [10].

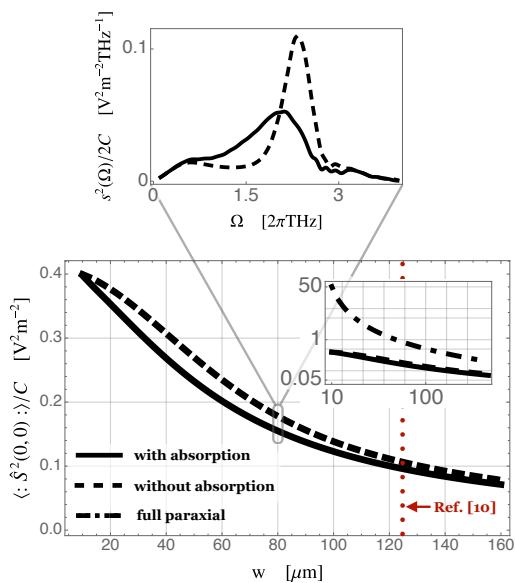


Figure 11. Comparison of the different approximated results II: Bottom: we numerically evaluate $\langle S^2(0,0) \rangle$ as functions of the beam waist w for the parameters realised in Ref. [10] using the different approximated results: The full-paraxial approximation (56), the laser-paraxial approximated result with absorption (59) and without absorption (53). The vertical red dotted line indicates the beam waist used in Ref. [10]. Top: spectrum of the electro-optic sampling signal for a beam waist $w = 80 \mu\text{m}$ using the laser-paraxial approximated result with (solid line) and without (dashed line) absorption. In both plots, the signals are normalised by $\sqrt{C} = 2\chi^{(2)}L\omega_c N/n\epsilon_0 c$.

with $\omega_{\text{TO}} = 5.31 \times 2\pi\text{THz}$, $\gamma = 0.09 \times 2\pi\text{THz}$, $C_0 = -0.07$, $r_{41} = 1.17 \times 10^{-21}\text{CV}^{-2}$. We further use the refractive index in the THz-frequency range as measured in Ref. [10] which is also shown here in Fig. 10. Compare Tab. I for an overview over all parameters.

Using these parameters we calculate again the electro-optic signal as a function of the beam-waist in the laser-paraxial approximation both with and without absorption (Eq. (59) and Eq. (53) respectively) as well as in the full paraxial approximation [Eq. (56)]. The result is shown in the bottom part of Fig. 11. In the inset we see that in this parameter range the paraxial-approximation does not apply since it overestimates the signal significantly (by up

to two orders of magnitude). Comparing the integrated signal $\langle S^2(0,0) \rangle$ with and without including absorption effects we see moderate differences of up to 15%. In the upper part of Fig. 11 the spectrum of the signal at $w = 80 \mu\text{m}$ is shown [remember that the spectrum is accessible via the two-beam setup, compare Eq. (35)]. Here, we see a clear difference between the results which include absorption effect or not: absorption effects give rise to additional contributions at around $1.5 \times 2\pi\text{THz}$ whereas the peak at around $2.2 \times 2\pi\text{THz}$ gets damped due to the increase of the imaginary part of the refractive index, compare Fig. 10. This shows the crucial importance of including absorption effects into the description of electro-optic sampling even when operating far from any material resonances. See also Sec. IV D and in particular Figs. 15 and 16 for a comparison of these theoretical predictions to the experimental data from Ref. [10]. Furthermore, here we only discussed values of the beam waist $w > 10 \mu\text{m}$ for which only propagating modes and not evanescent ones contribute. The importance of absorption effects becomes even more evident for $w < 10 \mu\text{m}$ where evanescent modes dominate the signal. This is discussed in the next section, since for $w < 10 \mu\text{m}$ the beam divergence has to be taken into account.

B. Beam divergence and beam-waist dependence of the signal

So far, we have assumed that the laser pulses have a Gaussian profile with constant beam width w . However, in a more realistic scenario the laser pulses are focused to a certain point inside the crystal and diverge over a certain length scale—the Rayleigh length z_R , cf. Fig. 8 (b). To account for this effect, we consider lowest order Laguerre-Gaussian modes which have the form [27]

$$\mathbf{E}_p(\omega, \mathbf{r}) = E_p(\omega) \sqrt{\frac{2}{\pi w^2}} \frac{e^{-r_{\perp}^2/w^2(1+iz/z_R)}}{1+iz/z_R} e^{ikz} \mathbf{e}_y. \quad (62)$$

Here, $z_R = kw^2 = \pi w^2/\lambda$ is the Rayleigh length where λ is the wavelength of the laser pulse. Note that by taking the limit $z/z_R \rightarrow 0$ in Eq. (62) we recover the Gaussian mode structure considered in Sec. IV A, cf. Eq. (44). This means, that the results obtained in the last section are only good approximations as long as the Rayleigh length is much larger than the length of the nonlinear crystal, i.e. $z_R \gg L$ or equivalently $w \gg \sqrt{L/k}$ as we will show explicitly in the following. However, since the signal increases with decreasing beam waist (compare Figs. 9 and 11) future experiments might strive for smaller values of w and thus the question arises in which way the signal is effected if $z_R \gg L$ does not hold anymore.

In this section we thus derive equations which take the beam divergence into account. Furthermore, we apply this formalism to the parameter range experimentally accessed in Ref. [10] except that we decrease the beam waist.

Inserting the more general shape of the laser pulse in Eq. (62) into the expression for the filter function found in Eq. (25), we find after some algebra

$$F_1(\mathbf{r}', \mathbf{r}'', \Omega) = \left(\frac{4|\chi^{(2)}(\Omega)|c\mu_0 N\omega_p}{w^2 n(\omega_c)} \right)^2 f(\Omega, \mathbf{r}) f^*(\Omega, \mathbf{r}') \times e^{-in_g \frac{\Omega}{c}(z' - z'')}, \quad (63)$$

where

$$f(\Omega, \mathbf{r}) = \frac{1}{2 \int_0^\infty d\omega \eta(\omega) E_p^2(\omega)} \int_0^\infty d\omega \frac{w^2}{\mathcal{W}^2(\omega, z)} \times E_p(\omega) E_p(\omega - \Omega) \text{Re}_\Omega \left[e^{-2r_\parallel^2 / w^2 (1 + i \frac{2zc}{n(\omega - \Omega)w^2})} \right]. \quad (64)$$

Here, we have defined

$$\mathcal{W}^2(\omega, z) = w^2 \left(1 + i \frac{2zc}{n(\omega - \Omega)w^2} \right), \quad (65)$$

and recall Eq. (46) for the definition of the modified real part Re_Ω . In a next step we insert Eq. (63) into Eq. (42) (note that we are using Eq. (42) instead of Eq. (26) in order to account for a possible lateral shift) and after a calculation very similar to the one in Sec. IV A one finds

$$s^2(\Omega, \delta \mathbf{r}_\parallel) = \frac{(N\omega_p)^2 \hbar}{16\pi^3 c^4 \epsilon_0^3 n^2(\omega_c)} |\chi^{(2)}(\Omega)|^2 \Omega^2 \int_0^\infty dq_\parallel q_\parallel \int_0^\infty d\omega \int_{-L/2}^{L/2} dz \int_0^\infty d\tilde{\omega} \int_{-L/2}^{L/2} dz' \frac{e^{-in_g \Omega(z - z')/c}}{[2 \int_0^\infty d\omega \eta(\omega) E_p^2(\omega)]^2} \times \text{Re} \left[g(q_\parallel, \delta \mathbf{r}_\parallel) \frac{e^{iq_z |z - z'|}}{q_z} \right] \text{Re}_\Omega \left[E_p(\omega) E_p(\omega - \Omega) e^{-q_\parallel^2 \mathcal{W}^2(\omega, z)/8} \right] \text{Re}_\Omega \left[E_p(\tilde{\omega}) E_p(\tilde{\omega} - \Omega) e^{-q_\parallel^2 \mathcal{W}^{*2}(\tilde{\omega}, z')/8} \right]. \quad (66)$$

One could in principle carry out the z and z' integrals in Eq. (66) straight away. Here, we first approximate in Eq. (65) by assuming that the central frequency of the laser pulse ω_c is much larger than the width of spectrum of the laser pulse σ and the resolved THz

frequency Ω , i.e. $\omega_c \gg \sigma, \Omega$ such that

$$\mathcal{W}^2(\omega, z) \approx w^2 \left(1 + i \frac{2zc}{n\omega_c w^2} \right). \quad (67)$$

This is a very accurate approximation for the setup used in Ref. [10] where $\omega_c = 375 \times 2\pi$ THz, $\sigma = 1.5 \times 2\pi$ THz and $\Omega < 3 \times 2\pi$ THz. Using Eq. (67) in Eq. (66) and assuming that the spectrum of the laser $E_p(\omega)$ is centred symmetrically around the central frequency, i.e. $E_p(\omega_c - \omega) = E_p(\omega_c + \omega)$ one finds

$$s^2(\Omega, \delta \mathbf{r}_\parallel) = \frac{(N\omega_p)^2 \hbar}{4\pi^3 c^4 \epsilon_0^3 n^2(\omega_c)} |\chi^{(2)}(\Omega)|^2 f^2(\Omega) \Omega^2 \int_0^\infty dq_\parallel \int_{-L/2}^{L/2} dz \int_{-L/2}^{L/2} dz' e^{-in_g \Omega(z - z')/c} q_\parallel e^{-q_\parallel^2 w^2/4} \times \text{Re} \left[g(q_\parallel, \delta \mathbf{r}_\parallel) \frac{e^{iq_z |z - z'|}}{q_z} \right] \text{Re} \left[e^{-iq_\parallel^2 zc/4n\omega_c} \right] \text{Re} \left[e^{-iq_\parallel^2 z'c/4n\omega_c} \right]. \quad (68)$$

Next, we carry out the z, z' integrals just as we did in Eq. (59). The resulting expression involves four different terms, each resembling that in Eq. (59) but with the phase mismatch replaced by

$$\Delta q = \pm q_z + n_g \frac{\Omega}{c} \rightarrow \pm q_z + n_g \frac{\Omega}{c} \pm q_\parallel^2 c/4n\omega_c. \quad (69)$$

Hence, including the beam divergence into the formalism leads to a new phase matching condition ($\Delta q = 0$) which involves a new term which grows quadratically

with q_\parallel .

To analyse this result we plot $\langle : \hat{S}^2(0, 0) : \rangle$ [recall $\langle : \hat{S}^2(0, 0) : \rangle = \int_0^\infty d\Omega s^2(\Omega)$] fixing all parameters as in Ref. [10] (compare Tab. I) except that we vary L/z_R by varying the beam waist w . The result shown in the left column of Fig. 12 reveals the dependence of the integrated signal on the beam waist and can be seen as an extension of Fig. 11 to lower values of the beam waist. As expected, we see that effects arising from the

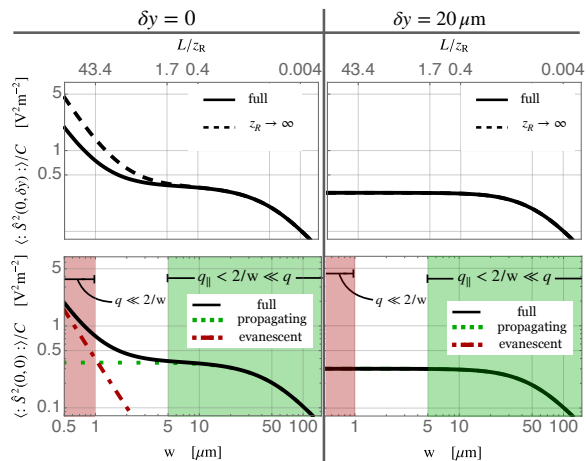


Figure 12. *Beam divergence*: First row: Using the parameters found in Table I the signal is calculated including [full, compare Fig. 8 (b)] and neglecting [$z_R \rightarrow \infty$, compare Fig. 8 (a)] the effect of the beam divergence. Second row: In the second row we show the signal including the effect of beam divergence as in the first row (full, black solid line), only including modes with $q_{\parallel} < \text{Re}[q]$ (propagating, green dotted line) and only including modes with $q_{\parallel} > \text{Re}[q]$ (evanescent, red dotted-dashed line). Note that in the bottom right plot the green dotted line cannot be seen since it overlaps entirely with the black solid line, whereas the red dotted-dashed line is negligibly small and thus cannot be found within the logarithmic scale shown here. In both rows the signal is calculated with a lateral shift between the two laser pulses of $\delta y = 0, 20 \mu\text{m}$ in the left and right columns, respectively.

divergence of the laser pulses arise only for $L/z_R > 1$. Furthermore, the signal can be characterized by two different regimes as indicated in the lower part of Fig. 12: for $2/w \ll q$ we find that only modes with $q_{\parallel} < \text{Re}[q]$ contribute since the exponential $e^{-q_{\parallel}^2 w^2/4}$ restricts the lateral component of the wave vector to $q_{\parallel} < 2/w$. These modes are propagating in z direction since in this case $q_z = \sqrt{q^2 - q_{\parallel}^2}$ has only a small imaginary part due to the small values of $\text{Im}[n(\Omega)]$, see Fig. 10. For $q \ll 2/w$, on the other hand, modes with $q_{\parallel} > \text{Re}[q]$ dominate the signal, compare the red dotted/dashed line in the lower left part of Fig. 12.

These modes are evanescent since now the imaginary part of $q_z = \sqrt{q^2 - q_{\parallel}^2}$ dominates over its real part.

In this regime the electro-optic signal grows exponentially with w again. Whenever absorption is neglected, evanescent modes get exactly cancelled such that the lateral wave vector is restricted to $q_{\parallel} < q$ [compare Eq. (53)] meaning that the behaviour of the signal in the regime $q \ll 2/w$ can only be modelled correctly if absorption effects are taken into account even though the resolved frequency range is far from any material resonance and the imaginary part of the refractive index remains below 0.15, see Fig. 10.

The exponential decay of the evanescent modes leads to an additional feature: when considering the two-beam setup with a finite lateral shift between the laser pulses which is big enough such that the two laser pulses do not overlap, we find that evanescent modes do not contribute anymore. This can be seen in the right part of Fig. 12 where we used the same parameters as before but chose a lateral shift of $\delta y = 20 \mu\text{m}$. Interestingly, since now only propagating modes with $q_{\parallel} < q$ can contribute to the signal, the additional term $q_{\parallel}^2 c/4n\omega_c$ in the phase matching condition in Eq. (69) remains small even if the beam waist is reduced further. Hence, the beam divergence does not play any role even if $L/z_R > 1$, compare upper right plot of Fig. 12.

C. Angled beams

In electro-optic sampling experiments of the quantum vacuum using the two-beam setup the two laser pulses are not perfectly parallel but propagate into slightly different directions defined by an angle α , compare Fig. 8 (c). In order to describe this effect we define two new coordinate systems whose coordinates are rotated in the yz plane by $\pm\alpha$, i.e.

$$\mathbf{r}_{\pm\alpha} = \begin{pmatrix} x \\ y\cos(\alpha) \pm z\sin(\alpha) \\ z\cos(\alpha) \mp y\sin(\alpha) \end{pmatrix}. \quad (70)$$

This way the calculation of the filter function in the rotated reference frames is equivalent to the one carried out in Sec. IV A and one finds

$$\langle \hat{S}_{\alpha}^2(\delta t, \delta \mathbf{r}_{\parallel}) \rangle = \frac{1}{2} \int_0^{\infty} d\Omega \int_0^{\infty} d\Omega' \int_{V_C} d^3 r' \int_{V_C} d^3 r'' \left[F_1(\mathbf{r}'_{\alpha}, \mathbf{r}''_{-\alpha}, \Omega) \langle \hat{E}_{\text{vac},x}(\mathbf{r}', \Omega) \hat{E}_{\text{vac},x}^{\dagger}(\mathbf{r}'' - \delta \mathbf{r}_{\parallel}, \Omega') e^{i\Omega' \delta t} \rangle \right. \\ \left. + F_1(\mathbf{r}'_{-\alpha}, \mathbf{r}''_{\alpha}, \Omega) \langle \hat{E}_{\text{vac},x}(\mathbf{r}' - \delta \mathbf{r}_{\parallel}, \Omega) \hat{E}_{\text{vac},x}^{\dagger}(\mathbf{r}'', \Omega') e^{-i\Omega' \delta t} \rangle \right]. \quad (71)$$

One can carry out the \mathbf{r}'_{\parallel} and \mathbf{r}''_{\parallel} integrals using

$$\int_{-\infty}^{\infty} dy' \int_{-\infty}^{\infty} dy'' e^{-2\{[\cos(\alpha)y' + \sin(\alpha)z']^2 + [\cos(\alpha)y'' - \sin(\alpha)z'']^2\}/w^2 + in_g \frac{\Omega}{c} \sin(\alpha)(y' + y'') + iq_y(y' - y'')} \\ = \frac{\pi}{2} \frac{w^2}{\cos^2(\alpha)} e^{-\frac{w^2}{4\cos^2(\alpha)} [q_y^2 + \sin^2(\alpha)n_g \Omega/c] - i \frac{\sin(\alpha)}{\cos(\alpha)} [n_g \frac{\Omega}{c} \sin(\alpha)(z' - z'') - q_y(z' + z'')]} \quad (72)$$

Using this result, some further algebra shows that

$$s_\alpha^2(\Omega, \mathbf{q}_\parallel) = \hbar \frac{\left(N\omega_p \Omega f(\Omega) |\chi^{(2)}(\Omega)|\right)^2 [2n_T(\Omega) + 1] e^{-\left[q_x^2 + \frac{q_y^2}{\cos^2(\alpha)} + n_g^2 \frac{\Omega^2}{c^2} \tan^2(\alpha)\right] w^2/4}}{2\pi^2 c^4 \varepsilon_0^3 n^2 \cos(\alpha)^2} \operatorname{Re} \left\{ \frac{e^{i\mathbf{q}_\parallel \cdot \delta \mathbf{r}_\parallel}}{q_z} \left(1 - \frac{q_x^2}{q^2}\right) \right. \\ \left. \times \left(\frac{iL \operatorname{sinc}[Lq_y \tan(\alpha)]}{q_z - q_y \tan(\alpha) - n_g \frac{\Omega}{c} \frac{\cos(2\alpha)}{\cos(\alpha)}} + \frac{e^{-iLq_y \tan(\alpha)} - e^{-iL\left[n_g \frac{\Omega}{c} \frac{\cos(2\alpha)}{\cos(\alpha)} + q_z\right]}}{\left[q_z - n_g \frac{\Omega}{c} \frac{\cos(2\alpha)}{\cos(\alpha)}\right]^2 - [q_y \tan(\alpha)]^2} \right) + (n_g, \alpha \rightarrow -n_g, -\alpha) \right\}, \quad (73)$$

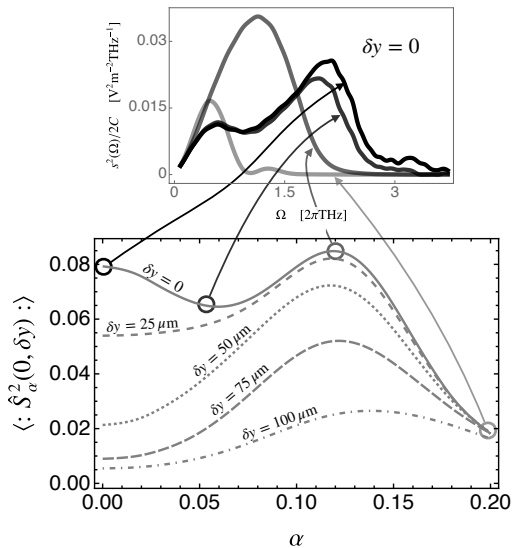


Figure 13. *Signal as a function of the angle α .* Bottom part: The signal as a function of α for the parameters in Table I is shown for different values of the lateral shift δy between the two laser pulses, compare Fig. 8 (c) for the definition of the angle α . Upper part: The spectrum of the signal at $\delta y = 0$ from the bottom plot for different values of the angle $\alpha = 0, 0.1, 0.15, 0.2$ as indicated by the arrows starting from the plot in the bottom.

and

$$\langle : \hat{S}_\alpha^2(\delta t, \delta \mathbf{r}_\parallel) : \rangle = \int d^2 q_\parallel \int_0^\infty d\Omega \cos(\Omega \delta t) s_\alpha^2(\Omega, \mathbf{q}_\parallel). \quad (74)$$

We use the result in Eqs. (73) and (74) to obtain the signal as a function of the angle α for different lateral shifts between the two laser pulses using the parameters realised in Ref. [10] (cf. Tab. I). The result is shown in Fig. 13. Note, that δy indicates the distance between the two laser pulses in the centre of the crystal, cf. Fig. 8 (c). With increasing angle α the two laser pulses get significantly closer than δy at the backside of the crystal. The bottom part of Fig. 13 can be explained by means of two effects.

Firstly, the phase matching condition now reads

$$\left[\cos(\alpha) q_z - \cos(2\alpha) n_g \frac{\Omega}{c} \right]^2 - [q_y \sin(\alpha)]^2 = 0. \quad (75)$$

With increasing angle α Eq. (75) can be satisfied for lower values of Ω leading to an increase of the signal for such values of Ω as can be seen in the spectrum in the upper part of Fig. 13.

Secondly, the signal decreases with decreasing overlap of the two laser pulses. This affects mainly the high frequency components of the signal which are more sensitive towards a longer propagation length. In case of $\delta y = 0$ an increasing angle α leads to less overlap and thus due to this effect the signal simply decreases with α . With increasing lateral shift δy on the other hand the signal starts to possess a maximum value when the angle is high enough such that the two laser pulses overlap again close to the backside of the crystal. This leads to an even higher increase of the signal obtained with a lateral shift $\delta y > 0$. For very high values of α the signals obtained using different lateral shifts δy are approximately the same since for all of them the two laser pulses cross somewhere within the crystal.

In the upper part of Fig. 13 we see the spectrum of the signal with $\delta y = 0$ for different values of α . We find that with increasing angle α the high-frequency components of the signal become suppressed. This will be further discussed when we compare our theory to experimental data in the following Sec. IV D.

D. Comparison to experimental data

We now compare the theoretical results obtained in the last sections to the experimental data taken from Ref. [10]. Here, the pulse duration δt and crystal length L are both much longer than in Ref. [9], being given by $\Delta t = 80$ fs and $L = 3$ mm, see Tab. I. This leads to the frequency range accessed using this experimental setup being much lower, given by $[0, 3] \times 2\pi$ THz. This means that thermal effects can become important, so should be discussed first. The ratio of thermal to quantum fluctuations is that of the two terms on the right hand side of Eq. (6), so is simply given by $2n_T(\Omega)$ as defined in Eq. (7). As shown in Fig. 14, the experiment of Ref. [9] mainly quantum fluctuations are accessed even at room temperature whereas in Ref. [10] one has to cool the system down to $T = 4$ K in order to observe a signal which is not dominated by thermal fluctuations.

To compare the theoretical framework developed here to the experimental data we adjust all parameters to agree with those used in Ref. [10], see Table I. As we can see from Fig. 11, in the parameter range of this experiment we cannot use the full paraxial approximation and also we have to include absorption effects. On the other hand, the experimentally re-

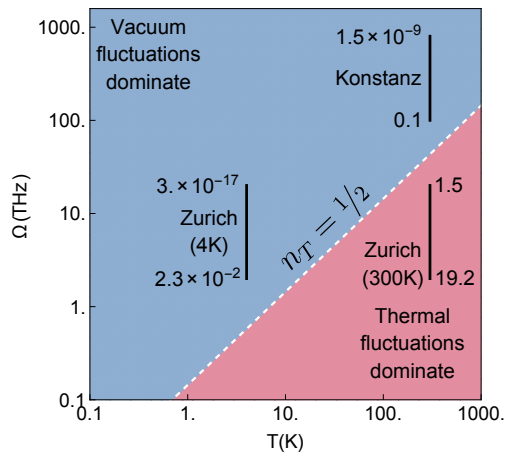


Figure 14. *Thermal versus quantum fluctuations*: Regions of the temperature-frequency parameter space in which each kind of fluctuation dominates, with the border defined by solving $2n_T(\Omega) = 1$. The frequency ranges access in Refs. [10] and [9] are indicated by the labels ‘Zurich’ and ‘Konstanz’, respectively, and the thermal photon number is shown at the end of each frequency range.

alised parameters lead to $L/z_R \approx 10^{-3}$ such that the effect of beam divergence can be neglected, compare Fig. 12. Hence, we use Eq. (59) which is the result in the laser paraxial approximation which includes absorption as well as Eq. (73) to account for the angle α between the laser pulses which we assume the be $\alpha = 0.05$. The results are shown in Fig. 15. We find reasonable agreement for frequencies $\Omega > 0.7 \times 2\pi$ THz given the uncertainties on parameters such as the nonlinear susceptibility and the group refractive index at $T = 4$ K. Also, the result which includes the the finite angle between the two laser pulses agrees better with the experimental data at high frequencies. The rather high values of the experimental data at low frequencies $\Omega < 0.7 \times 2\pi$ THz might indicate that the crystal or the surrounding optical instruments have not fully thermalised such that there are contributions stemming from a blackbody at $T = 20$ K, compare red dotted-dashed line in Fig. 15. Using $\alpha = 0.05$ and $T = 20$ K one finds good agreement between theoretical prediction and experimental data over the whole frequency range.

Next, we also compare the theoretical framework developed here to the measurement in Ref. [10] which includes lateral shifts between the two laser pulses, compare Fig. 16. Again, we find the best agreement for the result with $\alpha = 0.05$ and $T = 4$ K although the rather high experimental uncertainties cannot reliably distinguish between or rule out the different theoretical predictions.

Nevertheless, we have seen reasonable agreement between experimental data and the theoretical prediction and found that already in the measurements of Ref. [10] it is crucial to go beyond the paraxial approximation to the quantum vacuum and to include absorption effects. Also, effects arising from the angle between the laser pulses lead to changes in the signal of up to 0.15% and thus might be crucial to incorporate when future experiments further reduce the

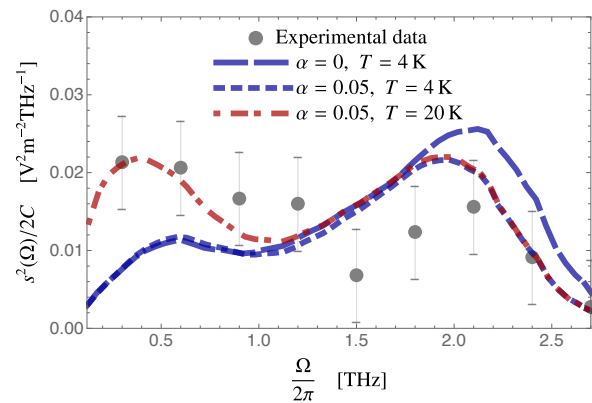


Figure 15. *Comparison to experimental data*.^a We plot the measurement data found in Ref. [10]. The predictions of our theoretical framework for different values of n_g are shown with the differently dashed lines. Here, $\sqrt{C} = 2\chi^{(2)}L\omega_p N/n\epsilon_0 c$.

^a We used a different Fourier transform convention for obtaining the spectrum from the time domain data compared to the one used in Ref. [10].

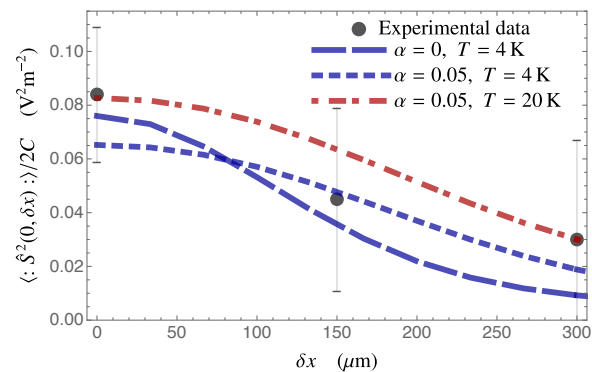


Figure 16. *Comparison to experimental data*.^a We plot the measurement data found in Ref. [10] with the solid line and its uncertainty is indicated by the shaded area. The predictions of our theoretical framework for different values of n_g are shown with the differently dashed lines. Here, $\sqrt{C} = 2\chi^{(2)}L\omega_p N/n\epsilon_0 c$.

^a We used a different normalisation for obtaining the spectrum from the time domain data as the one used in Ref. [10].

signal to noise ratio.

V. CONCLUSION

In this paper we have provided an in-depth discussion of the theoretical framework developed in Ref. [18] capable of predicting the quantised electromagnetic field behind a nonlinear crystal through which a coherent laser pulse propagates accounting for absorption, dispersion and possible reflective optical environments. This includes a new diagrammatic way of representing the resulting expressions for the electromagnetic field emerging from the crystal which makes it easier to apply this formalism to other processes such as spontaneous parametric down-conversion or the generation of photonic Bose-

Einstein condensates [14]. Furthermore, optical analogues of the dynamical Casimir force [40, 41] and of Hawking radiation [42] have recently been discussed. The description of these experiments and extensions thereof are also well suited to the formalism developed here. In all cases our formalism would allow for a discussion of these processes in a parameter regime where light and matter are strongly coupled or where the influence of surrounding optical objects (e.g. cavities) are non-negligible or even desired.

We extended the application of our theory to electro-optic sampling experiments compared to Ref. [18] by including angled-beams and effects stemming from the divergence of the laser pulses onto the output statistics. We further provided an in-depth discussion of the utility of different approximated results with the remarkable conclusion, that in experimentally relevant parameter regimes absorption has to be taken into account even when working far from any material resonance. Furthermore, a new relation was derived revealing that electro-optic sampling experiments can be used to access the two-point correlation function of the electric field operator as a function of its lateral wave vector. The approximated results showed reasonable agreement with experimental data.

Further investigations using this formalism are needed to find out if electro-optical sampling can be used to access the changes induced by macroscopic objects such as plates or cavities upon the quantum vacuum. This would form a link between the two ways of accessing the quantum vacuum: electro-optic sampling and more elaborate medium-induced quantum-vacuum effects such as the Casimir force, the Purcell effect or the Casimir-Polder force. Note that the effect of nonlinear processes upon the quantum vacuum itself has not been included so far, since these effects are expected to be much weaker than the one described in this paper. However, a useful generalization of this work would also include those effects [38, 39].

ACKNOWLEDGMENTS

The authors thank Stephen Barnett, Jonathan Brugger, Thomas Wellens, Vyacheslav Shatokhin, Giacomo Sorelli, Niclas Westerberg, Christoph Dittel, Jerome Faist, Ileana-Cristina Benea-Chelms, Francesca Fabiana Settembrini, Alexa Maria Herter, Denis Seletskiy, Guido Burkard and Alfred Leitenstorfer, for fruitful discussions. R.B. acknowledges financial support by the Alexander von Humboldt Foundation, S.Y.B. thanks the Deutsche Forschungsgemeinschaft (grant BU 1803/3-1476) and F.L. acknowledges support from the Studienstiftung des deutschen Volkes.

Appendix A: Green's tensor

In this appendix we give a brief introduction of the Green's tensor and the forms most convenient for this work. For a more detailed discussion see e.g. Ref. [16].

The Green's tensor \mathbf{G} is defined by Eq. (5) and the boundary condition $\mathbf{G}(\mathbf{r}, \mathbf{r}', \omega) \rightarrow 0$ for $|\mathbf{r} - \mathbf{r}'| \rightarrow \infty$. Here, $\varepsilon(\mathbf{r}, \omega)$ is the linear permittivity and c the speed of light in free space.

Neglecting reflection effects by assuming $\varepsilon(\mathbf{r}, \omega) = \varepsilon(\omega)$, the Green's tensor is given by its bulk case, defined as that which solves the differential equation (5) for $\varepsilon(\mathbf{r}, \omega) = \varepsilon(\omega)$. In a (2+1)-dimensional Weyl decomposition relative to a plane with normal vector in the positive z direction, one finds [16]:

$$\begin{aligned} \mathbf{G}^{(0)}(\mathbf{r}, \mathbf{r}', \omega) = & \\ & - \frac{1}{4\pi^2 k^2(\omega)} \int d^2 k_{\parallel} \frac{e^{i\mathbf{k}_{\parallel} \cdot (\mathbf{r} - \mathbf{r}')}}{k_z} \delta(z - z') \mathbf{e}_z \mathbf{e}_z \\ & + \frac{i}{8\pi^2} \int d^2 k_{\parallel} \frac{e^{i\mathbf{k}_{\parallel} \cdot (\mathbf{r} - \mathbf{r}')}}{k_z} \\ & \times \sum_{\sigma=s,p} \left[\mathbf{e}_{\sigma+} \mathbf{e}_{\sigma+} e^{ik_z(z-z')} \theta(z-z') \right. \\ & \left. + \mathbf{e}_{\sigma-} \mathbf{e}_{\sigma-} e^{-ik_z(z-z')} \theta(z'-z) \right]. \quad (\text{A1}) \end{aligned}$$

Here $k = \sqrt{\varepsilon(\omega)}\omega/c$ is the magnitude of the wave vector \mathbf{k} , and $k_z = k_z(k_{\parallel}, \omega) = \sqrt{k^2 - k_{\parallel}^2}$ with $\text{Im}[k_z] > 0$. The polarization vectors $\mathbf{e}_{\sigma\pm}$ with $\sigma = s, p$ are given by

$$\mathbf{e}_{s\pm}(\mathbf{k}_{\parallel}) = \mathbf{e}_{k_{\parallel}} \times \mathbf{e}_z = \frac{1}{k_{\parallel}} \begin{pmatrix} k_y \\ -k_x \\ 0 \end{pmatrix}; \quad (\text{A2})$$

$$\mathbf{e}_{p\pm} = \frac{1}{k} (k_{\parallel} \mathbf{e}_z \mp k_z \mathbf{e}_{k_{\parallel}}) = \frac{1}{k} \begin{pmatrix} \mp \frac{k_x k_z}{k_{\parallel}} \\ \mp \frac{k_y k_z}{k_{\parallel}} \\ k_{\parallel} \end{pmatrix}. \quad (\text{A3})$$

Appendix B: Vacuum Picture

We assume that the laser is in a coherent state such that its state is given by $|\{\mathbf{f}(\mathbf{r}, \omega)\}\rangle$ defined via $\hat{\mathbf{f}}(\mathbf{r}, \omega) |\{\mathbf{f}(\mathbf{r}, \omega)\}\rangle = \mathbf{f}(\mathbf{r}, \omega) |\{\mathbf{f}(\mathbf{r}, \omega)\}\rangle$ [43]. Note that we used the polaritonic annihilation operator $\hat{\mathbf{f}}$ to define the coherent state (instead of the usually used free-space creation and annihilation operators). The values for $\mathbf{f}(\mathbf{r}, \omega)$ can formally be defined assuming that the form of the classical laser pulse \mathbf{E}_p is known by demanding that the expectation value of the field operator $\hat{\mathbf{E}}$ coincides with the classical field, i.e.

$$\begin{aligned} \mathbf{E}_p = \langle \{\mathbf{f}(\mathbf{r}, \omega)\} | \hat{\mathbf{E}} | \{\mathbf{f}(\mathbf{r}, \omega)\} \rangle = & i \frac{\omega^2}{c^2} \sqrt{\frac{\hbar \varepsilon_0}{\pi} \text{Im} \varepsilon(\mathbf{r}, \omega)} \\ & \times \int d^3 r' \mathbf{G}(\mathbf{r}, \mathbf{r}', \omega) \cdot \mathbf{f}(\mathbf{r}', \omega). \quad (\text{B1}) \end{aligned}$$

Here we used that if there are no other excitations of the electromagnetic field apart from the laser pulse we have $\hat{\mathbf{E}} = \hat{\mathbf{E}}_{\text{vac}}$, where $\hat{\mathbf{E}}_{\text{vac}}$ is defined in Eq. (4). This way, the system is described by the state and field $|\{\mathbf{f}(\mathbf{r}, \omega)\}\rangle$, and $\hat{\mathbf{E}}_{\text{vac}}$, respectively. This means,

that the characterisation of the laser field is contained solely in the state of the system.

Equivalently, one can make use of a unitary transformation transforming the description of the laser pulse from the state of the electro-magnetic field to its field operator. This is done in close analogy to [28] except that here we have a continuous set of modes and use the polaritonic creation and annihilation operators instead of the free space ones. This transformation is performed by the following unitary operator;

$$\hat{\mathcal{D}}[\mathbf{f}(\mathbf{r},\omega)] = \exp \left\{ \int_{-\infty}^{\infty} d\omega \int d^3r \right. \\ \left. \times \left[\mathbf{f}(\mathbf{r},\omega) \cdot \hat{\mathbf{f}}^\dagger(\mathbf{r},\omega) - \mathbf{f}^*(\mathbf{r},\omega) \cdot \hat{\mathbf{f}}(\mathbf{r},\omega) \right] \right\}. \quad (\text{B2})$$

The transformed state then is given by the vacuum state of the theory which can be seen from

$$\hat{\mathbf{f}}(\mathbf{r},\omega) |\psi'\rangle = \hat{\mathbf{f}}(\mathbf{r},\omega) \hat{\mathcal{D}}^{-1}[\mathbf{f}(\mathbf{r},\omega)] |\psi\rangle = 0 \quad \forall, \quad (\text{B3})$$

for any $\hat{\mathbf{f}}(\mathbf{r},\omega)$ from which directly follows $|\psi'\rangle = |0_f\rangle$. Furthermore for the transformed field operator we find

$$\hat{\mathbf{E}}'(\mathbf{r},\omega) = \hat{\mathcal{D}}^{-1}[\mathbf{f}(\mathbf{r},\omega)] \hat{\mathbf{E}}(\mathbf{r},\omega) \hat{\mathcal{D}}[\mathbf{f}(\mathbf{r},\omega)] \\ = \mathbf{E}_p(\mathbf{r},\omega) + \hat{\mathbf{E}}_{\text{vac}}(\mathbf{r},\omega). \quad (\text{B4})$$

Here, $\hat{\mathbf{E}}_{\text{vac}}$ is given by Eq. (4).

In conclusion we find that the state and the operator of the electric field are transformed as

$$\{|\{\mathbf{f}(\mathbf{r},\omega)\}\}, \hat{\mathbf{E}}\} \rightarrow \{|0_f\rangle, \mathbf{E}_p + \hat{\mathbf{E}}_{\text{vac}}\}. \quad (\text{B5})$$

The latter is called the vacuum picture and is used throughout this work. In this picture the quantum field of the coherent laser pulse is given by the classical laser pulse and the vacuum electric field operator.

-
- [1] W. Heisenberg, *Zeitschrift für Phys.* **43**, 172 (1927).
[2] A. Einstein, *Phys. Z.* **18**, 121 (1917).
[3] P. W. Milonni, *The quantum vacuum: an introduction to quantum electrodynamics* (Academic press, San Diego, 2013).
[4] H. B. G. Casimir, *Proc. K. Ned. Acad. Wet.* **51**, 793 (1948).
[5] W. E. Lamb and R. C. Retherford, *Phys. Rev.* **72**, 241 (1947).
[6] J. L. Hemmerich, R. Bennett, and S. Y. Buhmann, *Nat. Comm.* **9**, 2934 (2018).
[7] E. M. Purcell, in *Confined electrons and photons* (Springer, 1995).
[8] H. B. G. Casimir and D. Polder, *Phys. Rev.* **73**, 360 (1948).
[9] C. Riek, D. Seletskiy, A. S. Moskalenko, J. Schmidt, P. Krauspe, S. Eckart, S. Eggert, G. Burkard, and A. Leitenstorfer, *Science* **350**, 420 (2015).
[10] I.-C. Benea-Chelmus, F. F. Settembrini, G. Scalari, and J. Faist, *Nature* **568**, 202 (2019).
[11] Q. Wu and X.-C. Zhang, *Appl. Phys. Lett.* **67**, 3523 (1995).
[12] Q. Wu and X.-C. Zhang, *Appl. Phys. Lett.* **68**, 1604 (1996).
[13] P. A. Franken, A. E. Hill, C. W. Peters, and G. Weinreich, *Phys. Rev. Lett.* **7**, 118 (1961).
[14] R. Nyman and M. Szymańska, *Phys. Rev. A* **89**, 033844 (2014).
[15] S. Scheel and S. Buhmann, *Acta Phys. Slovaca* **58**, 675 (2008).
[16] S. Y. Buhmann, *Dispersion forces I—macroscopic quantum electrodynamics and ground-state Casimir, Casimir–Polder and van der Waals forces* (Springer, Berlin/Heidelberg, Berlin, 2012).
[17] T. G. Philbin, *New J. Phys.* **12**, 123008 (2010).
[18] F. Lindel, R. Bennett, and S. Y. Buhmann, *Phys. Rev. A* **102**, 041701(R) (2020).
[19] B. Huttner and S. M. Barnett, *Phys. Rev. A* **46**, 4306 (1992).
[20] T. Gruner and D.-G. Welsch, *Phys. Rev. A* **53**, 1818 (1996).
[21] M.-S. Tomaš, *Phys. Rev. A* **51**, 2545 (1995).
[22] M. Kisliuk, *IEEE Trans. Microwave Theory Tech.* **28**, 894 (1980).
[23] L.-W. Li, P.-S. Kooi, M.-S. Leong, and T.-S. Yee, *IEEE Trans. Microwave Theory Tech.* **42**, 2302 (1994).
[24] Albert Einstein, *Akademie der Wissenschaft* **245**, 3 (1924).
[25] Bose, *Zeitschrift für Physik* **26**, 178 (1924).
[26] D. Polder and M. Van Hove, *Phys. Rev. B* **4**, 3303 (1971).
[27] R. W. Boyd, *Nonlinear optics* (Elsevier, San Diego, 2003).
[28] P. L. Knight and L. Allen, *Concepts of quantum optics* (Elsevier, 2013).
[29] A. N. Poddubny, I. V. Iorsh, and A. A. Sukhorukov, *Phys. Rev. Lett.* **117**, 123901 (2016).
[30] C. Riek, P. Sulzer, M. Seeger, A. S. Moskalenko, G. Burkard, D. V. Seletskiy, and A. Leitenstorfer, *Nature* **541**, 376–379 (2017).
[31] M. Kizmann, T. L. M. Guedes, D. V. Seletskiy, A. S. Moskalenko, A. Leitenstorfer, and G. Burkard, *Nat. Phys.* **15**, 960–966 (2019).
[32] H. Soo, and M. Krüger, *EPL* **115**, 41002 (2016).
[33] A. S. Moskalenko, C. Riek, D. V. Seletskiy, G. Burkard, and A. Leitenstorfer, *Phys. Rev. Lett.* **115**, 263601 (2015).
[34] M. Raymer, J. Cooper, H. Carmichael, M. Beck, and D. Smithey, *J. Opt. Soc. Am. B* **12**, 1801 (1995).
[35] W. Vogel and D.-G. Welsch, *Quantum optics* (John Wiley & Sons, 2006).
[36] D. T. F. Marple, *J. Appl. Phys.* **35**, 539 (1964).
[37] A. Leitenstorfer, S. Hunsche, J. Shah, M. C. Nuss, and W. H. Knox, *Appl. Phys. Lett.* **74**, 1516 (1999).
[38] S. Scheel and D.-G. Welsch, *Phys. Rev. Lett.* **96** (2006).
[39] J. A. Crosse and S. Scheel, *Phys. Rev. A* **81** (2010).
[40] S. Vezzoli, A. Mussot, N. Westerberg, A. Kudlinski, H. Dinparasti Saleh, A. Prain, F. Biancalana, E. Lantz, and D. Faccio, *Nat. Comm. Phys.* **2**, 84 (2019).
[41] N. Westerberg, A. J. Prain, D. Faccio, and P. Öhberg, *J. Phys. Comm.* **3**, 065012 (2019).

- [42] F. Belgiorno, S. L. Cacciatori, M. Clerici, V. Gorini, G. Ortenzi, L. Rizzi, E. Rubino, V. G. Sala, and D. Faccio, [Phys. Rev. Lett.](#) **105** (2010).
- [43] S. Fuchs, R. Bennett, and S. Y. Buhmann, [Phys. Rev. A](#) **98**, 022514 (2018).